Stony Brook University

Stress-assisted Grain Growth in Nanocrystalline Metals Inhibited by Grain Boundary

Segregation

A Thesis Presented

by

Yang Zhang

to

The Graduate School

in Partial Fulfillment of the

Requirements

for the Degree of

Master of Science

in

Department of Materials Science and Engineering

Stony Brook University

August 2015

The Graduate School

Yang Zhang

We, the thesis committee for the above candidate for the

Master of Science degree, hereby recommend

acceptance of this thesis.

Dr. Jason Trelewicz
Assistant Professor, Department of Materials Science and Engineering

Dr. Dilip Gersappe
Professor and Graduate Program Director, Department of Materials Science and Engineering

This thesis is accepted by the Graduate School

Charles Taber

Dean of the Graduate School

Abstract of the Thesis

Stress-assisted Grain Growth in Nanocrystalline Metals Inhibited by Grain Boundary Segregation

By

Yang Zhang

Master of Science

In

Department of Materials Science and Engineering

Stony Brook University

2015

Stress-assisted grain growth in nanocrystalline metals transpires collectively with a number of competing deformation mechanisms. In this study, molecular dynamics simulations of surface nanoindentation were performed to quantify the plastic strain distribution among competing mechanisms as a function of grain size and temperature during stress-assisted grain growth in nanocrystalline Ni and a Ni-1 at. % P alloy. Under identical conditions of rate and temperature in nominally the same grain size structure, stress-assisted grain growth found to be prevalent in pure nanocrystalline Ni was virtually absent in the Ni-P alloy with P enriched grain boundaries. A reduction in the deformation temperature also quelled mechanical grain growth in both nanocrystalline Ni, suggesting thermal activation was inherent to the governing physics. Plastic strain was found to be highly localized in the grain boundaries during nanoindentation, and dislocation activity while present, did not represent the dominant carrier of plasticity but an opponent factor against grain growth.

Table of Contents

Nanocrystalline Materials

Overview

Since the end of the last century, Ultrafine-Grained (UFG) materials (with average grain sizes of 100~1000 nm) and nanocrystalline (NC) materials (with average grain sizes of 1~100 nm) have been the subject of widespread research on their very different, usually enhanced properties and unique preparation processes. As grain size decreases, the atomic fraction of grain boundary atoms increases [Figure.1]. Likewise, the volume fraction of intercrystal regions and triple-junctions [Figure.2] increases. Consequently, UFG/NC materials are structurally distinct in comparison with their conventional polycrystalline counterparts, which has direct implications for structural stability and macroscopic properties such as strength/hardness, toughness, elastic modulus, ductility, diffusivity, and magnetic properties.[1-6]
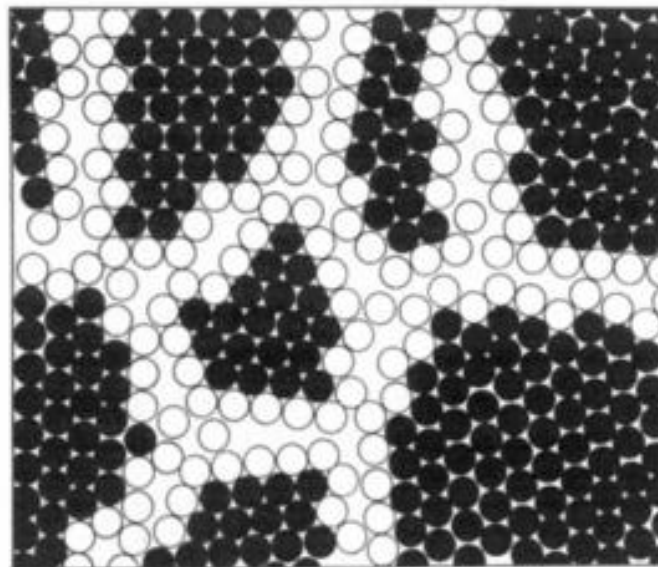

Figure 1　Two-dimensional model of a nanostructured material. The atoms in the centers of the crystals are indicated in black. The ones in the boundary core regions are represented as open circles. [From M. J. Weins, H. Gleiter and B. Chalmers, J. appl. Phys. 42, 2639 (1971)[7]]
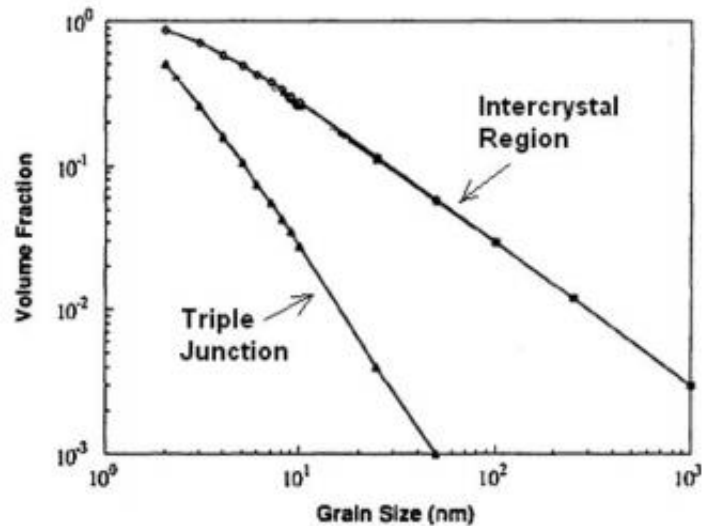
Figure 2　The effect of grain size on calculated volume fractions of intercrystal regions and triple junctions, assuming a grain-boundary thickness of 1 nm [From Palumbo G, Thorpe SJ, Aust KT. / Scripta Metall Mater 1990;24:1347–50 [8]]

Yield Strength

It is noted that most low-temperature, permanent deformation of metals is related to the movement of dislocations through grains in the metal.[9] That movement will result in permanent distortion of the grain itself, which is known as plastic deformation. When dislocations multiply in the structure, plastic deformation will be the dominant deformation mode and is irrecoverable upon unloading.

The impingement of dislocations at grain boundaries can produce dislocation multiplication if the grain boundary misorientation can accommodate cross-slip; however, these boundaries often inhibit cross-slip [cf. figure.3], in turn leading to a strengthening effect.　Thus, if a structure contains more grain boundaries (i.e. finer grained material), it will be difficult for dislocations to multiply in comparison to other coarse grained structures, and the structure will have a higher yield point. [figure.4] For curves A (d=27 μm), B (d=1 μm), C (d=200 nm), and E (d=18 nm), as the grain size decreases, the yield strength increases, [10] generally called Hall–Petch relationship.
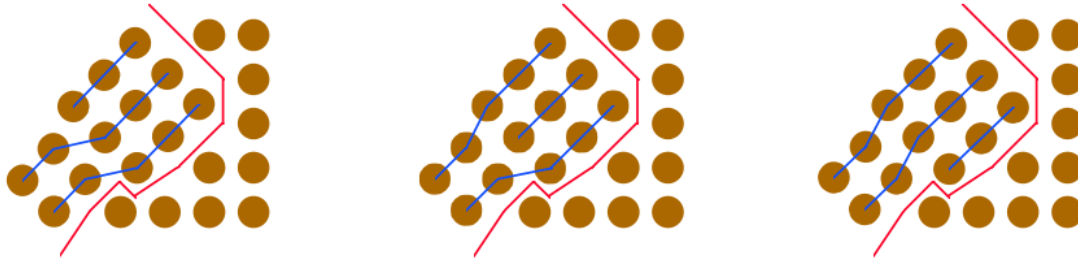
Figure 3 Representation of a Dislocation Stopped by a Grain Boundary [From Mike Gedeon / Brush Wellman's Alloy Customer Technical Service Department [11]]
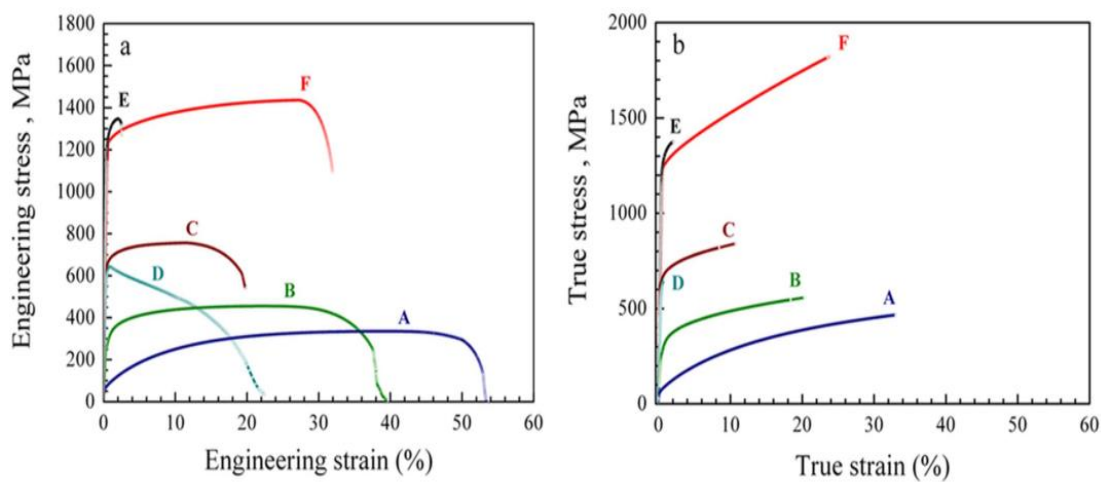
Figure 4   Tensile stress-strain curves of Ni. **(a)** Engineering stress-strain curves at a strain rate of 4×10^{-4} s^{-1}; **(b)** True stress-strain curves, converted using standard equations (up to the maximum stress point where non-uniform elongation onsets) from the corresponding curves in (a). **Curve A**: as-annealed coarse-grained (CG) Ni with an average grain size (d) of *27 μ m*. **Curve B**: electrodeposited (ED) Ni (*d = 1 μ m*). **Curve C**: electrodeposited ultrafine-grained (UFG) Ni (*d = 200 nm*); **Curve D**: UFG Ni obtained via equal channel angular pressing (ECAP) for one pass; **Curve E**: ED nanocrystalline Ni (d_{grain} = 18 nm); **Curve F**: electroplated nanodomained Ni (d_{grain} = 150 nm, d_{domain} = 7 nm) [From Xiaolei Wu, Fuping Yuan, et. al. / SCIENTIFIC REPORTS | 5:11728 | DOI: 10.1038/srep11728 [10]]

This kind of relationship between grain size and yield strength can be described as[12]:

$$\sigma = \sigma_0 + Kd^n \qquad (1)$$

where d is the mean grain size, σ is the yield strength, σ_0 is the lattice friction stress, K is a proportionality constant, and n is the grain size exponent (generally 0.3 – 0.5).

Ductility

Grain size refinement can make crack multiplication more difficult and therefore increase the fracture toughness in conventional grain size materials. However, the mechanisms responsible for the large increases in yield strength, such as inhibited dislocation cross-slip, can lead to the development of stress concentrations in the nanocrystalline structure. These stress concentrations promote premature fracture prior to the accumulation of any sizable amount of plastic strain, thus limiting the ductility of these high strength materials. This is reflected by the reduced elongation to failure in figure 4 as grain size is reduced below 100 nm.
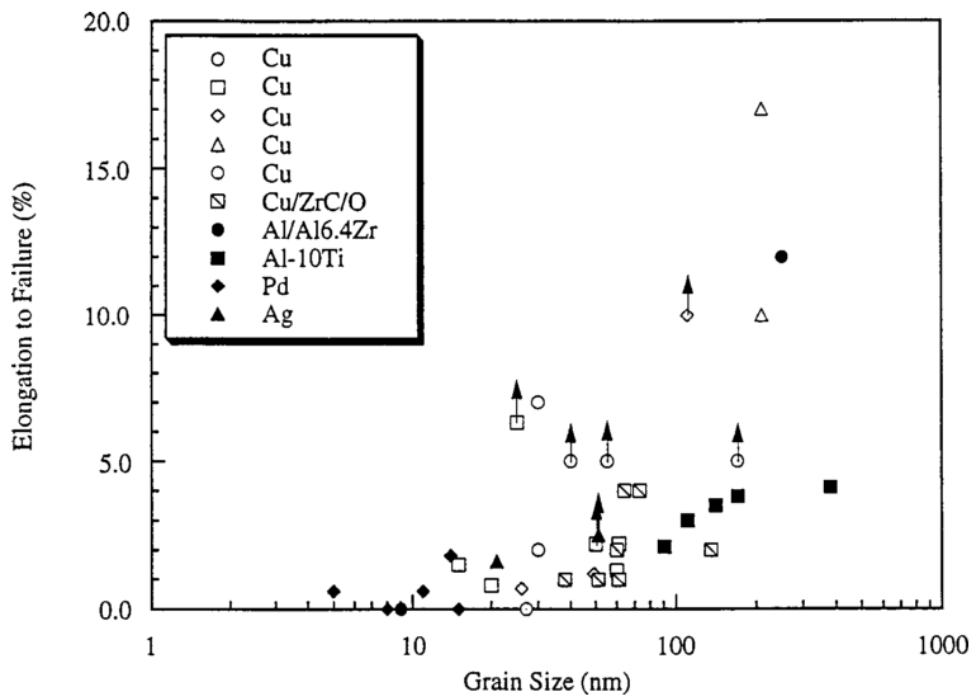
Figure 5   Elongation to failure in tension vs. grain size for some nanocrystalline metals and alloys. [From C. Suryanarayana and C.C. Koch / Hyperfine Interactions 130: 5–44, 2000[13]]

Superplasticity

Superplasticity is the ability of a material to sustain large plastic deformation at temperatures

greater than 0.5 T_m (T_m is the melting point of the matrix) for a stable fine-grained microstructure. Low-temperature superplastic behavior can be observed in nanocrystalline nickel, nanocrystalline aluminum alloy (1420-Al), and nanocrystalline nickel aluminide (Ni$_3$Al). [14] However, this behavior often derives from coarsening of the nanocrystalline structures at these elevated temperatures. Thus, the as-processed grain sizes for the nickel, 1420-Al, and Ni$_3$Al of 20nm, 100nm and 50 nm, respectively, increase during the thermomechanical testing.

Figure 6   Stress-strain curves for electrode-deposited nickel (a), aluminum alloy 1420-Al processed by severe plastic deformation (b), and Ni$_3$Al processed by severe plastic deformation (c) [From S.X. McFadden, et al. / Nature 398 1999 doi:10.1038/19486[14]]
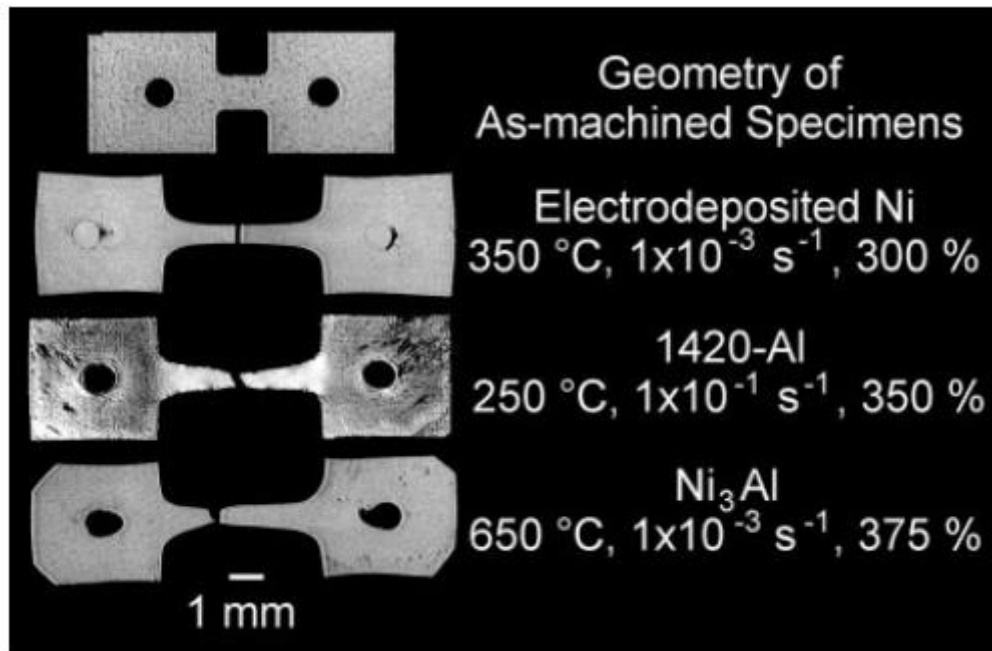
Figure 7　Miniature tensile specimens, shown in the as-machined geometry, and after deformation [From S.X. McFadden, et al. / Nature 398 1999 doi:10.1038/19486]
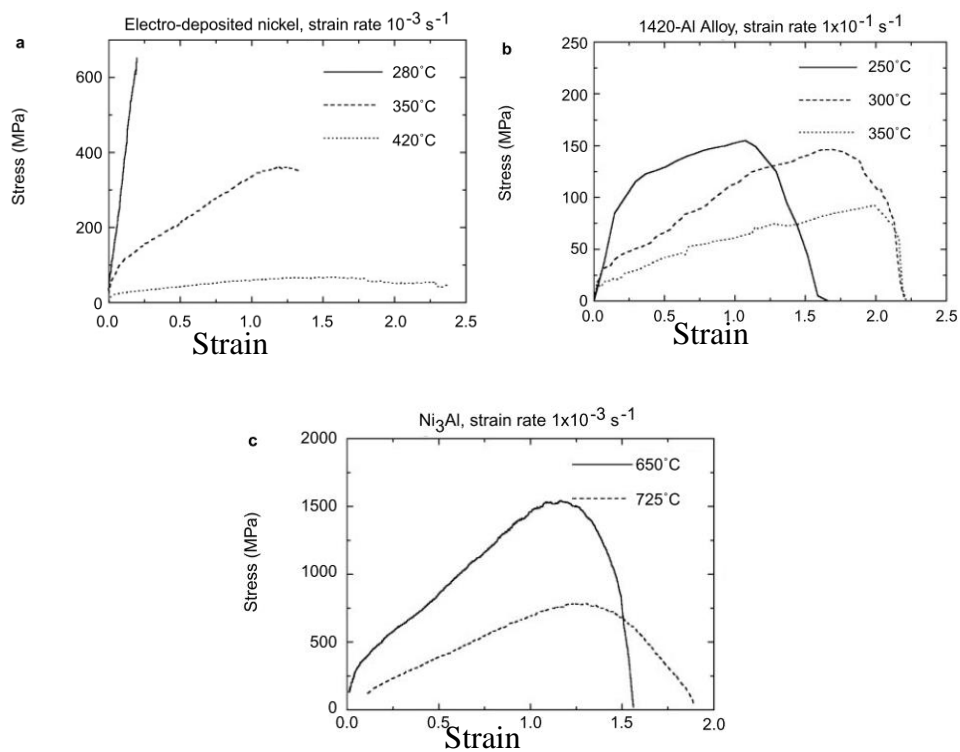
Synthesis

The synthesis and processing of nanocrystalline materials are also unique, and often require far-from-equilibrium processing conditions. Nanostructured materials have been synthesized in recent years by methods including inert gas condensation, mechanical alloying, spray conversion processing, severe plastic deformation, electrodeposition, rapid solidification, physical vapor deposition, chemical vapor processing, co-precipitation, sol-gel processing, sliding wear, spark erosion, plasma processing, auto-ignition, laser ablation, hydrothermal pyrolysis, thermophoretic forced flux system, quenching the melt under high pressure, biological templating, sonochemical synthesis, and devitrification of amorphous phases. [1, 13, 15-17] Inert gas condensation, mechanical alloying/milling, spray conversion processing, electrodeposition, and devitrification of amorphous phases are some of the more popular techniques used in the recent decade o produce nanocrystalline materials.

6

Methods to synthesize nanocrystalline materials.

Starting phase	Technique	Dimensionality of product
Vapor	Inert gas condensation	3D
	Physical vapor deposition – Evaporation and sputtering	1D
	Plasma processing	3D
	Chemical vapor condensation	3D, 2D
	Chemical reactions	3D
Liquid	Rapid solidification	3D
	Electrodeposition	1D, 3D
	Chemical reactions	3D
Solid	Mechanical alloying/milling	3D
	Devitrification of amorphous phases	3D
	Spark erosion	3D
	Sliding wear	3D

Figure 8   Some of the most common used to produce nanocrystalline materials and also the dimensionality of the product obtained. [From C.Suryanarayana and C.C.Koch / Hyperfine Interactions, 2000. 130[13]]

Inert Gas Condensation

Inert gas condensation can be used to produce very fine-grained alloys with selected substrate temperature and other operating conditions. First, evaporation of a metal occurs inside a very high vacuum chamber of about 10^{-5} Pa, followed by back filling to a low pressure gas (typically a few hundred Pa of helium). The evaporated metal atoms collide with the He atoms inside the chamber, lose their energy, and condense into the form of small, discrete crystals of loose powder.[15] This process is used to produce 3D nanocrystallites that contain grains of a few nanometers with a narrow size distribution. The crystal size is dependent upon the inert gas pressure, the evaporation rate, and the gas composition. Under certain configurations, extremely fine particles can be produced.
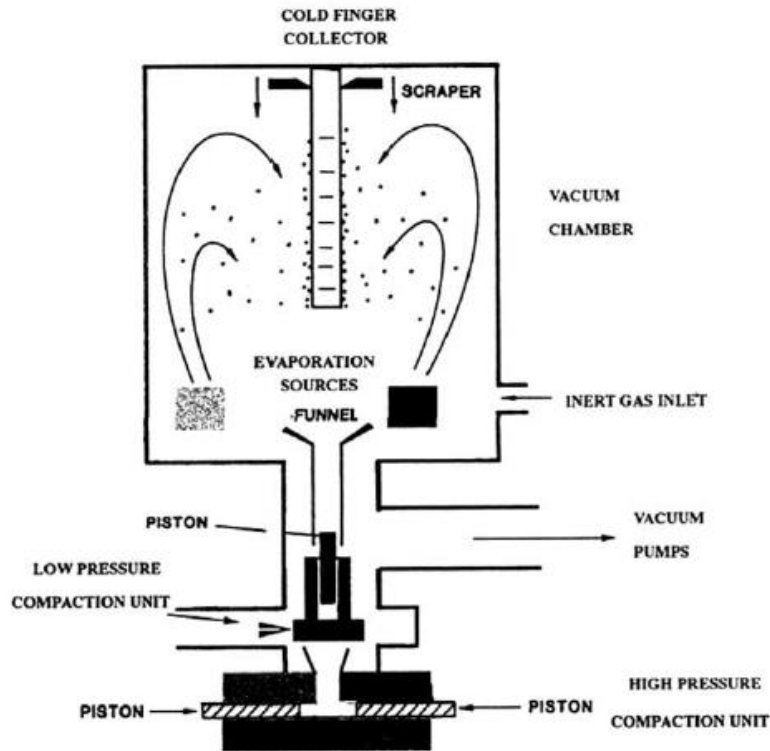
Figure 9   Schematic drawing of the inert gas condensation technique. [From Morris DG. Mechanical behavior of nanostructured materials. Trans Tech Publication Ltd; 1998.[18]]

Mechanical Alloying

Mechanical alloying produces nanoscale materials by deforming coarser grained powders through a localized severe plastic deformation (SPD) process. Mechanical alloying consists of repeated welding, fracturing, and rewelding of powder in a dry high-energy ball mill until the desired composition is achieved. In this process, mixtures of elemental or pre-alloyed powders are subjected to grinding under an inert atmosphere in equipment capable of high-energy compressive impact forces such as attrition mills, shaker mills and ball mills. It has been shown that nanometer-sized grains can be obtained in almost any material after sufficient milling time. The grain sizes were found to decrease with increasing milling time down to a minimum value that seemingly scale inversely with the melting temperature.[19] Contamination is usually of concern in this process, especially when reactive metals and/or long milling times are involved.[19]

8
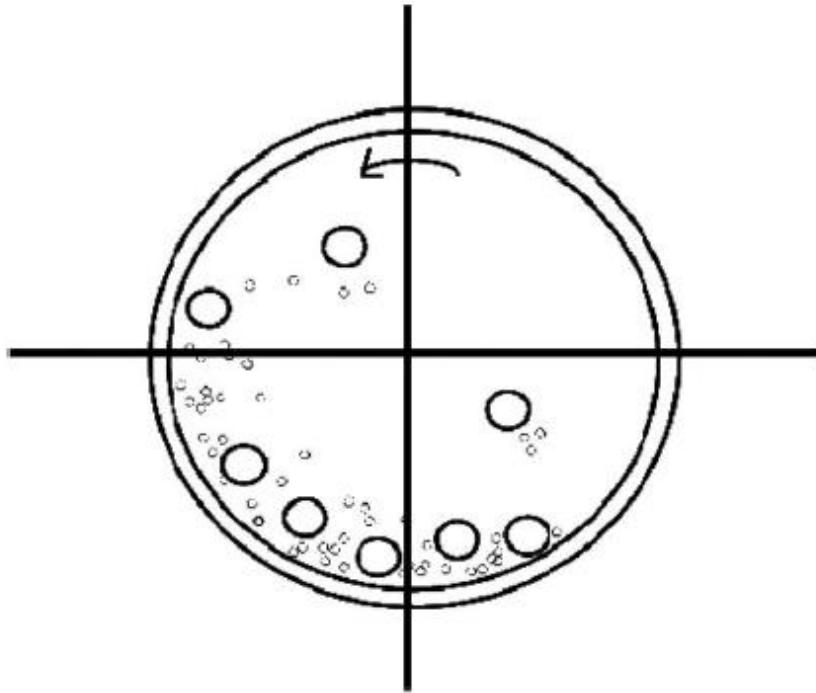
Figure 10   Schematic drawing of mechanical alloying technique. [From M.A. Meyers et al. / Progress in Materials Science 51 (2006)[5]]

Electrodeposition

The electrodeposition technique has significant advantages over other methods for synthesizing nanocrystalline materials: (1) potential of synthesizing a large variety of nano-grained materials—pure metals, alloys and composite systems with grain sizes as small as 20 nm, (2) low investment, (3) high production rates, (4) few size and shape limitations, and (5) high probability of transferring this technology to existing electroplating and electroforming industries.

It has been shown that electrodeposition yields grain sizes in the nanometer range when the electrodeposition variables (e.g., bath composition, pH, temperature, current density, etc.) are chosen such that nucleation of new grains is favored rather than growth of existing grains. In the pulsed electrodeposition technique, modulated AC signals can be used to control the composition and grain size of the product.
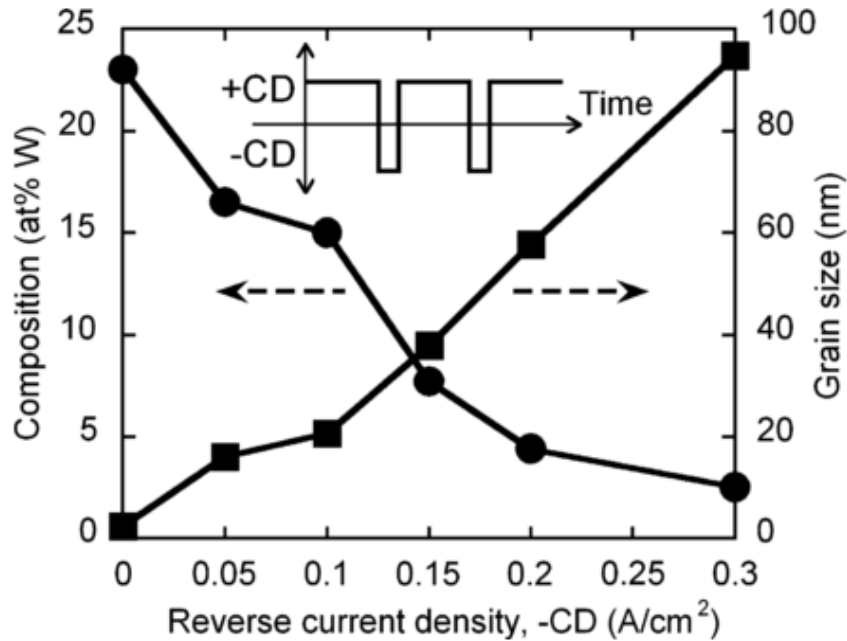
Figure 11   The effect of adding a periodic reverse (anodic) pulse during the electrodeposition of Ni–W on the composition and, in turn, grain size of the alloy. [From A.J. Detor, C.A. Schuh / Acta Materialia 55 (2007)[20]]

Severe Plastic Deformation

The use of severe plastic deformation (SPD) for the processing of bulk ultrafine-grained materials is now widespread. This technique utilizes mechanical energy to refine the microstructural length scales, and UFG grain sizes in the range of 200-500 nm can be achieved. Numerous techniques for SPD processing are now available; the major methods are high-pressure torsion (HPT), equal-channel angular pressing (ECAP), accumulative roll-bonding (ARB).

ECAP uses a plunger to press a rod-shaped billet through a die constrained within a channel that is bent at an abrupt angle. A shear strain is introduced when the billet passes through the point of intersection of the two parts of the channel. Since the cross-sectional dimensions of the billet remain unchanged, the pressings may be repeated to attain exceptionally high strains and ultimately a UFG structure.

HPT refers to processing in which the sample, generally in the form of a thin disk, is subjected to torsional straining under a high hydrostatic pressure. Plastic torsional straining is achieved by rotation of one of the anvils.

ARB makes use of a conventional rolling facility. A sheet is rolled to one-half the thickness in a pre-rolled condition, followed by cutting into two halves and stacked together, then rolled again to one-half thickness repeatedly.
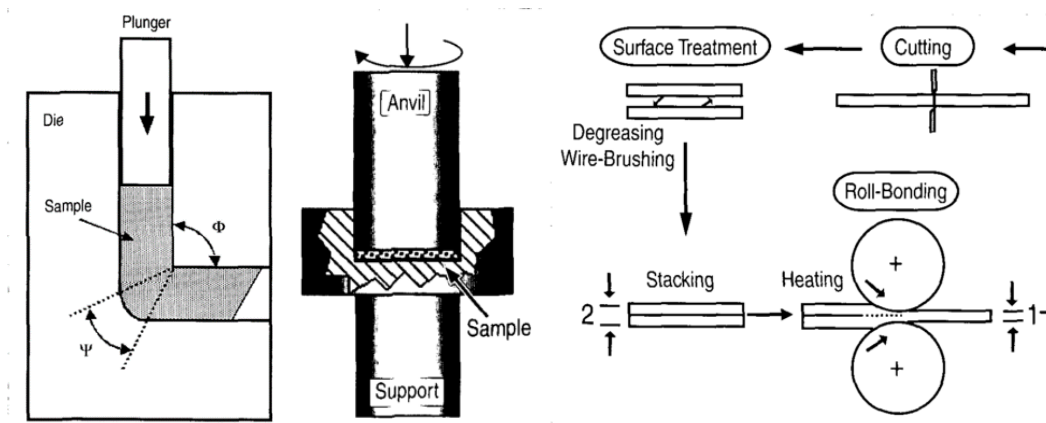
Figure 12　Schematic drawing of ECAP, HPT, ARB respectively. [From R.Z. Valiev et. al. / JOM 2006[21]]

Applications

Based on the unique properties discussed above and many other magnetic, thermal, optical, and chemical properties, several potential applications have been identified for nanocrystalline materials including dispersions and coatings, high surface area materials, functional nanostructures (e.g., optoelectronic devices, biosensors, nanomachines) and bulk nanostructured materials for structural or magnetic applications, which are described further below.

Structural Application

It has been known that the fracture toughness of ceramics can be considerably enhanced by

dispersing in them in a second phase on a microscopic scale. The reduction of grain size can lead to the increase in strength and hardness, thus superstrong and supertough ceramics are achievable with the fabrication of micro and nanohybrids.

Nanostructures can also be utilized as wear-resistant and thermal barrier coatings. A nanocrystalline nickel coating on Nd-Fe-B hard magnets provided wear and corrosion resistance. Due to the small grain size and increased phonon scattering at grain and layer boundaries, nanocrystalline barrier coatings should adhere better and at the same time exhibit reduced thermal conductivity. Ultimately, the nanocrystalline coating can be applied to improve the wear-resistance and retain a tough interior under relatively low-temperature circumstances.

Magnetic Applications

The phenomenon of giant magnetoresistance (GMR) in nanomaterials have been used for information storage systems. In the area of permanent magnet materials, nanocrystalline materials provide flexibility in manufacturing and reduction of materials cost. In the area of soft magnetic materials, "finemet" and "nanoperm" nanocrystalline / amorphous Fe-based alloys have performed exceptionally well in transformer cores, data communication interface components, sensors, common mode choke coils, and magnetic shielding. The Magnetocaloric effect can be applied to magnetic refrigeration to avoid the use of harmful chlorofluorocarbons.[22-28]

Chemical Applications

Due to their large surface area, nanocrystalline materials can be used for catalysis purposes, and several studies have shown that the catalytic activity and selectivity can be dependent on particle size. Metal hydrides provide a tradeoff between safety, efficiency, and cost for hydrogen storage. Nanocrystalline materials exhibit increased solubility at low pressure, narrowed miscibility gap, lowered plateau pressure, and disappearance of transformation to

other metal hydride phases compared to coarse-grained alloys, since the high density of grain boundaries and interfaces might increase diffusion. A final noteworthy advantage is that the powder does not comminute as the result of repeated hydrogen charging-discharging.

Concluding Remarks of This Section

Nanocrystalline materials are potentially high impact materials for many uses, not only scientifically, but also practically, and there are still a number of technological applications being explored. Their exceptional properties differ from their conventional coarse-grained polycrystalline counterparts, and more efficient mass production will further enhance their utility for new technology applications.

Grain Growth Mechanisms

Since polycrystalline materials are in the metastable state, grain growth will occur to decrease the interfacial energy and hence the total energy of the system. In NC materials, the existence of high density grain boundaries and interfaces provides a higher driving force and hence a higher tendency to grow.

However, under the metastable state, Nanocrystalline materials also need activation energy to initiate changes. In this section, thermal stability and stress-assisted grain growth will be discussed.

Thermal Stability

Isothermal grain growth mechanisms on the microscale can be described by the function[16]:

$$d^n + d_0^n = Kt \tag{2}$$

where d is the grain size at time t, d_0 is the initial grain size, and n is the grain growth

exponent. K is a constant related to activation energy Q and temperature T:

$$K = K_0 exp\left(\frac{-Q}{RT}\right) \tag{3}$$

K_0 is a pre-exponential constant and R is the gas constant.

Based on functions (2) and (3), as the temperature goes up, time needed for the structure to grow from d_0 to d will be shortened. And let $d = (1+x)d_0$:

$$t = \frac{d_0^n[1+(1+x)^n]}{K} \tag{4}$$

For finer grained materials and a fixed x, much less time is needed. The observed grain growth exponent n in nanocrystalline materials has been found to vary from low values of 2 to as high as 10, while for coarse-grained materials the value is generally 2, deduced from a parabolic relationship. Although n was found to vary in different systems, for large normalized temperature value T/Tm, $1/n$ generally increases toward ideal 0.5, Tm is the melting point, i.e. n is decreasing while T increases. [Figure.13]

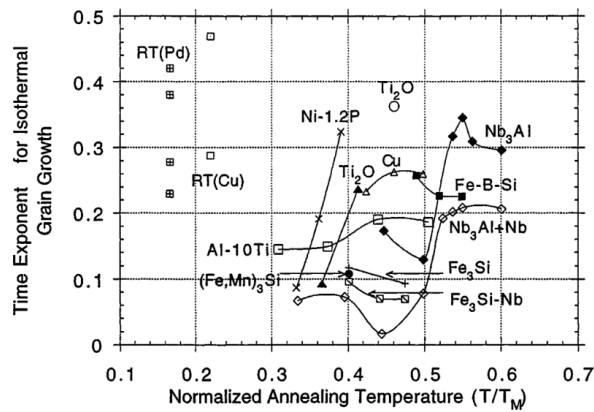Figure 13　Time exponent, 1/n for isothermal grain growth of various nanocrystalline materials as a function of the annealing temperature. [C. Suryanarayana, C.C. Koch / Nanocrystalline materials[13]]

As is shown by function (4), for fixed d_0, d, and K, $t \propto a^n$ which means it will need more time to grow if n is larger.

Thus, for function (2), the following conclusion can be made: smaller initial grain size structures at high temperature grow faster than larger initial grain size structures at low temperature.
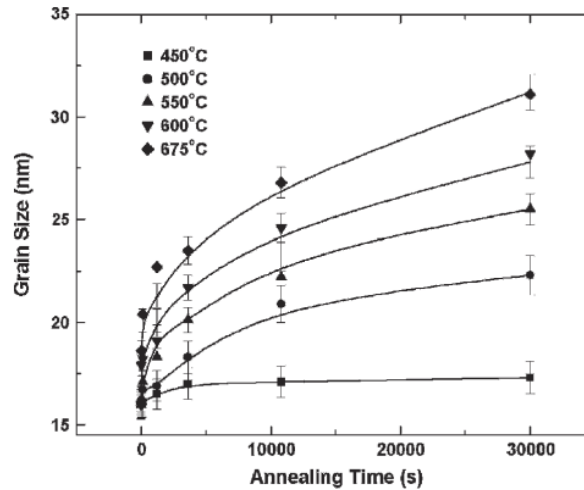

Figure 14　Grain size as a function of annealing time in the temperature range of 450℃ to 675℃ for Ti. [From F.Sun, et al. , METALLURGICAL AND MATERIALS TRANSACTIONS A 37A, 2006[29]]

Activation energy (Q) data for grain growth in nanocrystalline materials have been compared with activation energy for lattice (Q_l) and grain boundary diffusion (Q_{gb}) in order to determine the underlying mechanisms.[30] In reference [5] most of the results on Q for nanocrystalline materials compare better with Q_{gb} rather than Q_l, although there are several exceptions to declare that the grain growth is not a simple mechanism. Thus, depending on the alloy system under consideration, grain growth in nanocrystalline materials may appear to have a close relationship with lattice diffusion, grain boundary diffusion, or crystallization of amorphous phases.[1, 16]

However, as a metastable state, nanocrystalline materials prepared by any method grow very slowly up to a reasonably high temperature. It has been suggested that the resistance to grain growth results from an insufficient driving force[31] to overcome the barriers created by a narrow grain size distribution, equiaxed grain morphology, low energy grain boundary

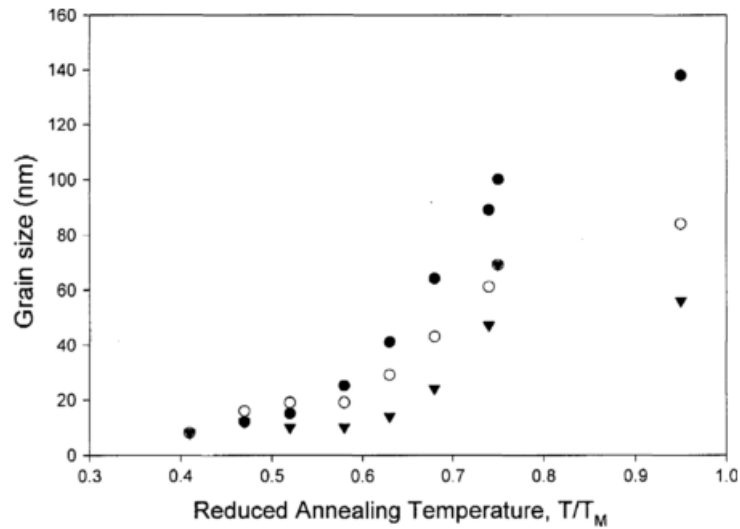structures, relatively flat grain boundary configurations, and porosity.

Figure 15　Grain size versus reduced annealing temperature (T/TM) for nanocrystalline Pd–Zr alloy. ●Pd-15 at.% Zr; ○Pd-19 at.% Zr; ▼Pd-20 at.% Zr. [From Hiroaki Okamoto, Phase Diagrams for Binary Alloys, ASM International, 2000[32]]

Also, as shown in Figure.15, solute segregation to the grain boundaries will limit nanocrystalline grain growth. Grain boundary segregation may lower the grain boundary energy sufficiently to forbid grain growth, since this will reduce the driving force. This effect was discussed in $Pd_{1-x}Zr_x$ alloy systems by reference [33], and more detailed discussed by reference [34].

Stress-assisted Grain Growth

Thermodynamic factors are not the only factors that will influence grain growth. In recent years, an in situ deformation test with a transmission electron microscope was conducted to investigate the deformation mechanisms in Ultrafine / Nanometer grained materials. Stress-assisted grain growth is commonly observed. A direct observation of grain growth during nanoindentation at room temperature has been published assuming that the stress / deformation will accelerate the grain growth process or provide a different way for grain coarsening. Some

explanations have been proposed, however the detailed mechanisms haven't yet been confirmed.
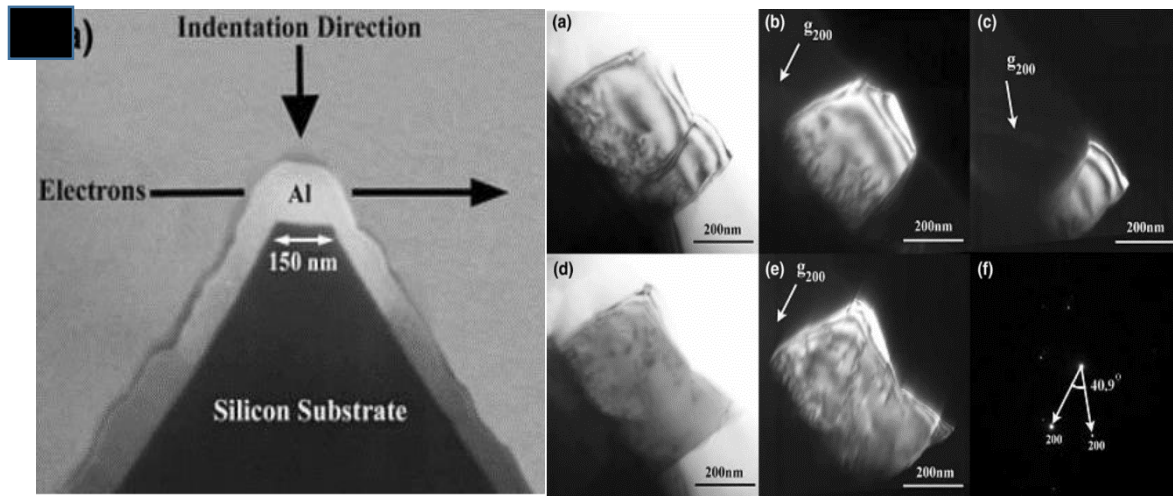

Figure 16   Sectional view of nanoindentation on Al with TEM (left) and grain growth observed (right). (a) Bright-field image before the indentation; (b) dark-field image of the larger grain before the indentation; (c) dark-field images of the smaller grain before the indentation; (d) bright-field image after the indentation; (e) dark-field image of the larger grain after the indentation, showingthe larger grain grew by eliminating the smaller grain; (f) diffraction pattern before the indentation, showing the high angle grain boundary between the two grains at the start. [From M. Jin et al. / Acta Materialia 52 (2004)[35]]

In Figure.16, (a) shows that there are two grains in the initial structure, and (b) (c) (f) shows the 2 grains are of different orientation. (d) and (e) show that after nanoindentation two grains coalesce into one, and figure.16 indicates that the grain growth is related to orientation changes, i.e. grain rotation.

Figure.17 seems to show a different mechanism, grain 1 is separately distributed into grain 2, and grain 3, making both of them grow and finally overlay each other. This appears to be the long-discussed grain boundary migration; however, there is no clear evidence indicating the detailed mechanism during the growth.

Stress-assisted grain growth has also been observed in a hot extrusion experiment with a TEM and an Atom-Probe Tomography analysis on a UFG Al alloy [36]. The results not only show

the grain growth during deformation (Figure.18), but also the solute segregation in grain boundaries which reduces the GB energy (Figure.19).
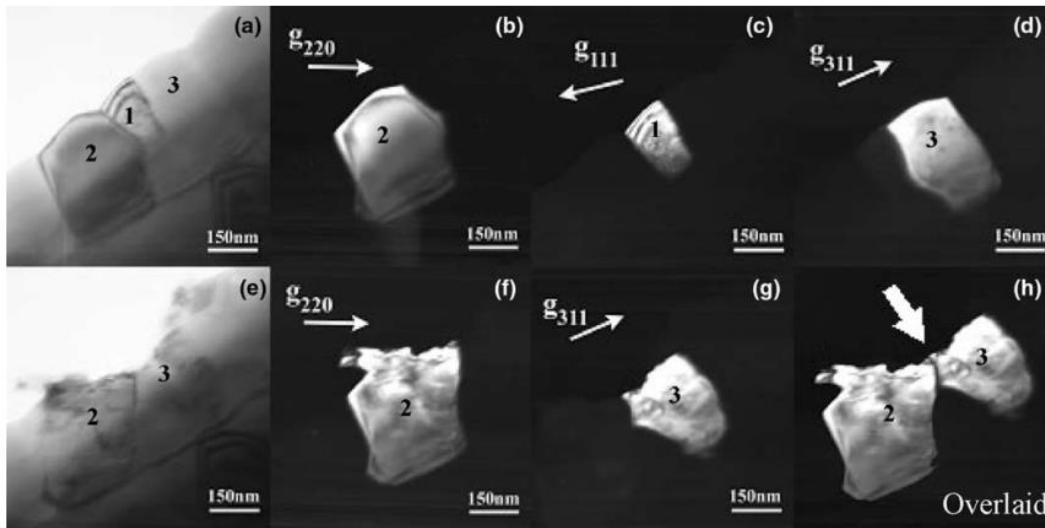
Figure 17　(a) Bright-field image before the indentation, showing three grains numbered as 1, 2, and 3; (b)–(d) dark-field images of grain 2, grain 1 and grain 3 before the indentation, respectively; (e) bright-field image after the indentation; (e) and (f) dark-field images of grain 2 and grain 3 after the indentation respectively; (h) the two Dark-field images, (f) and (g), overlaid, showing that grain 1 has been eliminated by the two grains beside it. [From M. Jin et al. / Acta Materialia 52 (2004)[35]]
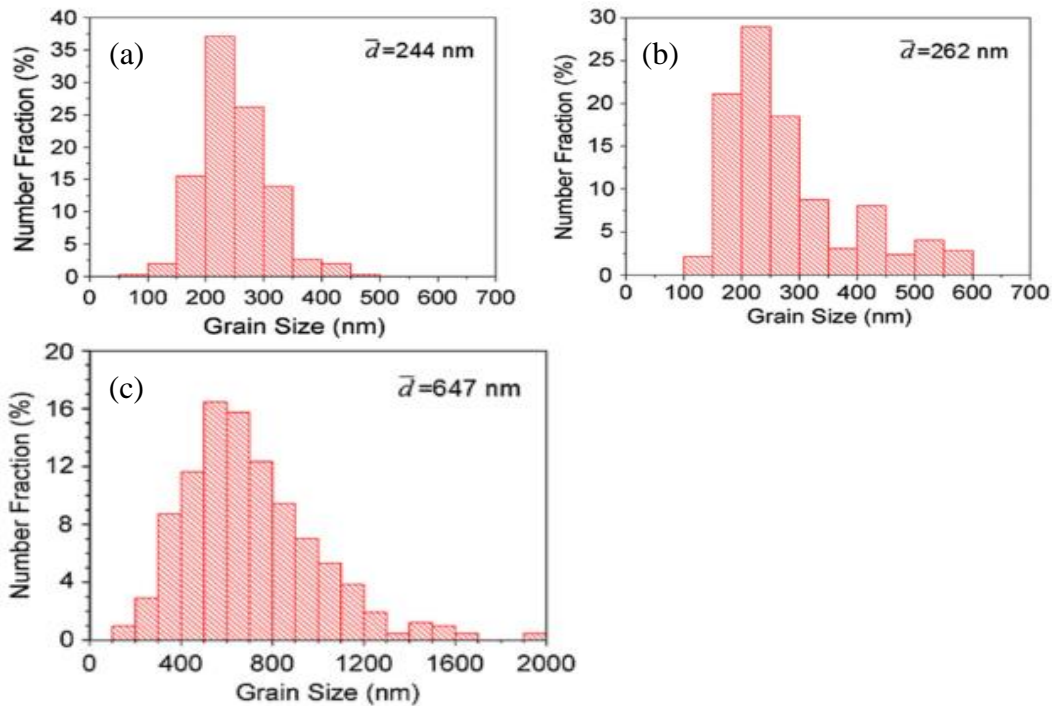
Figure 18   Grain size distribution of the Al alloy. (a) as-Hot-Isostatic-Pressed (as-HIPped), (b) as-annealed at 673K for 5 hours, (c) after extrusion: ~2.9 seconds with a strain rate of ~0.8 s^{-1}. [Lin, Y., et al. / Metallurgical and Materials Transactions A, 45 2014[36]]
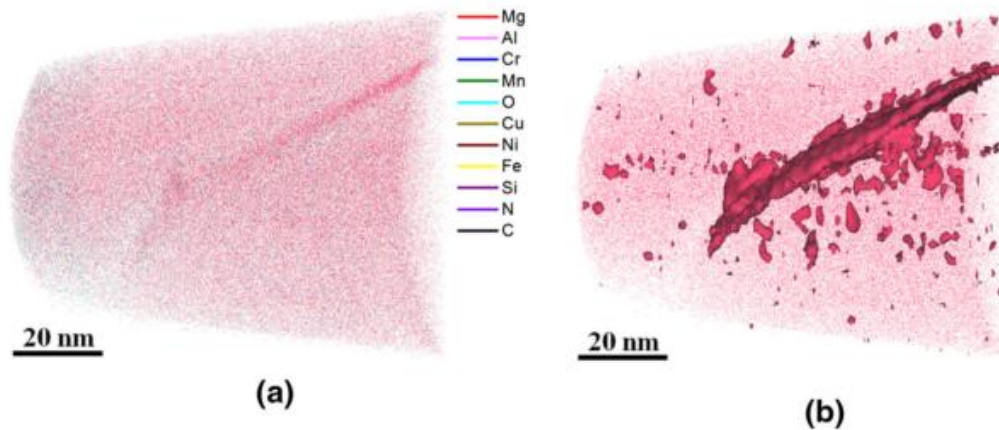

Figure 19   APT analysis results of the hot extruded Al alloy. (a) a typical tomographic 3D reconstruction (9 million atoms in reconstruction) with atoms of all elements displayed in different colors, where a GB is included, (b) Mg atoms in the reconstruction with 6 at. % Mg isoconcentration surface superimposed, which delineates the GB. [Lin, Y., et al. / Metallurgical and Materials Transactions A, 45 2014[36]]

However, as the author noted, "GB segregation occurring during hot extrusion can be considered to be of an equilibrium nature, which is primarily related to temperature."

For all the stress-assisted grain growth observations described above, the time for deformation is extremely short (several seconds), compared to temperature driven grain growth (several hours). Thus, stress-assisted grain growth is much more rapid than temperature driven growth.

Atomistic Computational Simulation

Limited by characterization techniques and equipment, detailed mechanisms cannot be observed directly or clearly. However, by the means of atomistic simulations, it is possible to analyze anything with qualitative accuracy because the structure is built atom by atom. Thus, the atomistic simulation is a useful way to study atomic scale mechanisms of different kinds of materials.

Advantages and Disadvantages

It is clear that atomistic simulations will help us understand the atomic scale mechanisms taking place during annealing, deformation, or any other process by examining the visible (structure, solute distribution, dislocations etc.[37]) or invisible (atomic stress, atomic strain, deformation gradient, potential energy etc.[38]) properties.

Another advantage is efficiency, both time and investment. The equipment associated with atomic scale testing, especially those with in-situ analysis attachments, is extremely expensive and requires extensive training. The experiment cycle for doing a complete analysis using expensive equipment would be at least several months, taking queuing time into account. Atomistic simulations do not have those problems since the clusters and supercomputers are now accessible at a considerably low cost. The experiment cycle will be days or weeks based on the size of simulated structure and the CPUs used.

Although atomistic simulations have all these advantages, its disadvantage is also obvious: all of the rules in the simulation world are written by scientists, i.e. only those phenomena within the range of reliable theoretical descriptions are testable, however, in atomic scale it is without a 100% confidence to say that the science understood everything. Besides, all the computational experiments are conducted in a relatively ideal state, so there could be something beyond the experimental settings. Thus, only when real experiments prove the idea, the idea can be confirmed.

Taking all of this into consideration, atomistic simulations are best for conducting pioneer work and initial analysis to light up the field and blow away some of mist.

Basic Procedures

In comparison to real experiments, atomistic simulations should follow certain procedures:

choosing potential, building structure, setting experiment configurations, visualization and data analysis.

Choosing Potential

Potential files are designed to describe interatomic interactions.

Since the accuracy of the simulation is based mainly on potentials, it is important to choose a reliable and optimized potential for each type of bond. Potentials are usually generated and tested by first principle calculations, based on some vital properties of the elements such as lattice structure, modulus matrix, etc.

Generally, generating a reliable potential requires arduous efforts and special techniques, which is far beyond the scope of this article. Luckily, most of the common elements and some of the common alloys' potentials have already been documented and published. Although simulations are limited by the potential library, researchers still have some of flexibility with choosing potentials to fit their purpose.

Building Structure

Building the initial sample structure is much like constructing a block, usually the nanocrystalline structure is generated from a Voronoi tessellation:

1. Define the shape and size of the sample

2. Spread some random organized seeds in the basic shape.

3. Construct Voronoi cells

4. Fill the Voronoi cells with organized atoms (FCC, BCC etc.) with desired distribution of grain orientations.

5. Delete the atoms that overlay others.

A GNU licensed simple code to construct FCC NC rectangular structures can be found on the website https://code.google.com/p/fillatoms/ [39]. And through simple modifications, the code can be used to generate BCC or other cubic system structures.

Setting Experiment Configurations

After the initial structure is constructed, the simulation experiment can start. Choose one of the molecular dynamics (MD) simulation platforms that contains the features needed to complete the experiment, then write the script based on the rules given by the platform to set up the experiment.

 # general variables

variable   temperature equal 700

variable   size equal 10

variable   nsteps_run equal 100000

 # variables for 'fix sgcmc'

variable   nsteps_mc   equal 100

variable   swap_fraction equal 0.2

variable   temperature_mc equal $temperature

variable   deltamu equal -0.70

variable   target_concentration equal 0.02

variable   kappa equal 1e3

 # general settings

units   metal

atom_style   atomic

```
# set up structure

boundary          p p p

lattice           bcc 2.88

region            box block 0 $size    0 $size    0 $size

create_box        2 box

create_atoms      1 box

reset_timestep    0

timestep          0.0025

# set up interaction

pair_style        eam/fs

pair_coeff        * * FeCu.pasianot.eamfs Fe Cu

# initialize velocities

variable          double_temp equal $temperature*2

velocity          all create $double_temp 428459 dist gaussian

# what and how to run

fix               integrate all npt temp $temperature $temperature 1.7 aniso 0.0 0.0 1.5

fix               mc all sgcmc $nsteps_mc $swap_fraction $temperature_mc $deltamu
randseed 324234 variance $kappa $target_concentration

# set up output

thermo            10

thermo_style      custom step temp atoms pe press lx ly lz f_mc[1] f_mc[2] f_mc[3] f_mc[4]

thermo_modify     flush yes

dump              1 all custom 2000 mc.*.dump id type x y z

run               $nsteps_run
```

The above is a sample script used in LAMMPS (Large-scale Atomic/Molecular Massively Parallel Simulator). The script generates a Fe-Cu alloy and then performs a Scalable Parallel Monte Carlo algorithm to get the precipitation, and finally, outputs all atoms with atom id, type, and position.[40]

Data Analysis

Data analysis is analogous to the microscope and works similar to other characterization techniques on nanoscale materials. Through the statistical calculation of various atomic configurations, the nanostructure and its evolution can be characterized.

There are all kinds of metrics exhibiting all kinds of behaviors an atom portrays. In most cases, the metrics are only related to the position of the atom, its neighbor, and the potentials. In this article, the most important deformation metrics will be discussed.

There are all kinds of counting methods that will give us a clear view of what we want to see, such as layer analysis, section analysis, and other classifications of atoms. In general cases, grain boundaries and grain interiors will be examined respectively, since their behavior contrast each other.

Metrics and Algorithms

To understand what happens in the structure, some analysis tools are needed to depict the structure (lattice matrix, grain boundaries, and dislocations) and the deformation processes (translation, rotation and dilatation). As a result, the common neighbor analysis, the atomic deformation gradient, the green strain tensor, and micro-rotation are designed.

Common Neighbor Analysis

A popular method of complex, high-dimensional signatures to characterize arrangements of

atoms is known as the common neighbor analysis (CNA). CNA does not directly take the spatial vectors between two neighbors into account. Instead, a characteristic signature is computed from the topology of bonds that connect the surrounding neighbor atoms.
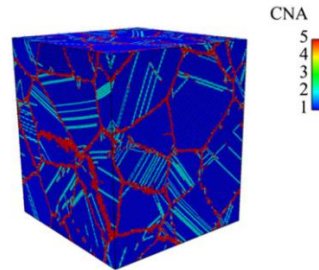

Figure 20　Snapshots of 15nm grained NC Cu at 10% tensile strain colored by CNA. [From: G.J. Tucker et al. / J. Mech. Phys. Solids 60 (2012)[41]]

To get the CNA value of an atom, 3 steps need to be performed:

1. Determine the neighbors using a cut-off radius:

    The cut-off radius varies for different structures: for close packed structures (FCC, HCP) the cutoff distance is set to be halfway between the first and second neighbor shell, giving for FCC:

$$r_{cut}^{FCC} = \frac{1}{2}\left(\sqrt{1/2} + 1\right)a_{FCC} \approx 0.854 a_{FCC}$$

    Where a_{FCC} is the lattice constant of the FCC structure.

    For a BCC structure, two neighbor shells need to be taken into account, and atoms are considered to be bonded with their first and second-nearest neighbors:

$$r_{cut}^{BCC} = \frac{1}{2}\left(1 + \sqrt{2}\right)a_{BCC} \approx 1.207 a_{BCC}$$

    Where a_{BCC} is the lattice constant of the BCC structure.

2. Compute 3 characteristic numbers for each neighbor bond of the central atom.

Three numbers are computed for each of the N neighbor bonds of the central atom:

The number of neighbor atoms, the central atom, and its bonded neighbor have n_{cn} in common.

The total number of bonds between these common neighbors, n_b;

The number of bonds in the longest chain of bonds connecting the common neighbors, n_{lcb}.

This yields N triplets (n_{cn},n_b,n_{lcb}), for FCC and HCP, N = 12; for BCC, N = 14.

3. Compare all characteristic number sets of all neighbor bonds with reference sets to get an idea of which class the central atom will be assigned to.

fcc ($N = 12$)	hcp ($N = 12$)	bcc ($N = 14$)	cubic diamond ($N = 16$)
$12 \times (421)$	$6 \times (421)$	$8 \times (666)$	$12 \times (543)$
	$6 \times (422)$	$6 \times (444)$	$4 \times (663)$

CNA signatures of common crystal structures. For example: An hcp-coordinated atom has six bonds of type (421) and six bonds of type (422). That is, any two near-neighbors in an hcp crystal have exactly four common neighbors, which are interconnected by two bonds. And the longest continuous chain these two bonds form is either of length one or two (in six cases each).

Slip Vector

CNA is capable and can classify many structures, however it also has its limitations: CNA can only show a static state, and fails to capture those that have undergone deformation or slip. The slip vector is mainly used to classify dislocations, both partial and full dislocations.
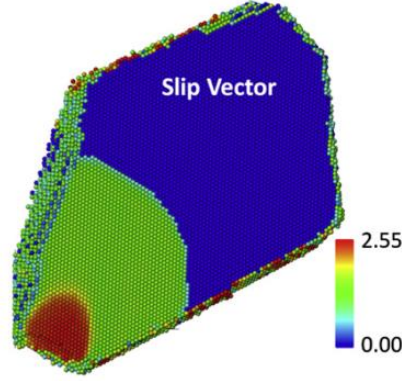
Figure 21   Dislocation emission in tensile testing simulation colored by slip vector value. The leading and trailing partial dislocations are separated by a stacking fault, and atoms behind the trailing partial have undergone full slip. [From: G.J. Tucker et al. / J. Mech. Phys. Solids 60 (2012)[41]]

The slip vector can be calculated as:

$$s^\alpha = -\frac{1}{n_s}\sum_{\beta \neq \alpha}^{n}\left(x^{\alpha\beta} - X^{\alpha\beta}\right)$$

where s^α is the slip vector of atom a, n is the number of nearest neighbors(β), n_s is the number of slipped neighbors, and $x^{\alpha\beta}$ and $X^{\alpha\beta}$ represent the interatomic distance vectors between atom α and neighbor β in the current and reference configurations, respectively. Therefore, the slip vector defines the deformation of an atom's neighborhood by calculating the slip of its nearest neighbors with respect to the reference configuration.

Deformation Gradient

To investigate the kinematics of deformation within the NC structures, an atomic deformation gradient (**F**) was formulated in reference[42] and [43]. Their results show that deformation gradients and the metrics derived from them can provide valuable nanoscale information regarding interfacial and bulk lattice deformation. In addition, the use of certain metrics outlined in this work provide insight into the deformation history of atomic fields during straining, and illustrate a significant advantage over traditionally utilized metrics in atomistic
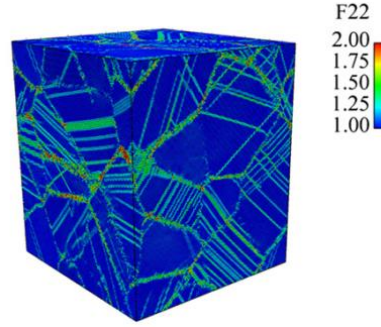
simulation analysis.

Figure 22   Snapshots of 15nm grained NC Cu at 10% tensile strain colored by Deformation Gradient in 22 direction. [From: G.J. Tucker et al. / J. Mech. Phys. Solids 60 (2012)[41]]

The atomic deformation gradient (**F**) for an atom α, according to each neighbor β in the neighbor list, is estimated from a least squares error minimization approach as:

$$(\omega^\alpha)_{iM} = (F^\alpha)_{iI}(\eta^\alpha)_{IM} \quad or \quad (F^\alpha)_{iI} = (\omega^\alpha)_{iM}(\eta^\alpha)_{MI}^{-1}$$

Where $\quad (\omega^\alpha)_{iM} = \sum_{\beta=1}^{n}(x^{\alpha\beta})_i(X^{\alpha\beta})_M$

And $\quad (\eta^\alpha)_{IM} = \sum_{\beta=1}^{n}(X^{\alpha\beta})_I(X^{\alpha\beta})_M$

In these equations, upper case letters refer to quantities in the reference configuration, while lower case letters refer to those in the current configuration; i, I, and M are direction notions (1 or 2 or 3).

Micro-Rotation

Once the deformation gradient is calculated, by separating **F** into the stretch tensor (**U**) and the Rotation Tensor (**R**), we will be able to investigate exactly how the space around the central atom deformed, including how much it stretched and how much it rotated.
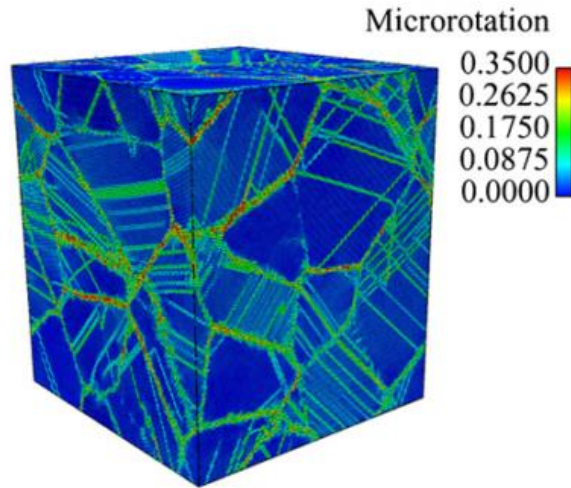
Figure 23 Snapshots of 15nm grained NC Cu at 10% tensile strain colored by Micro-rotation. [From: G.J. Tucker

et al. / J. Mech. Phys. Solids 60 (2012) [41]]

Based on the following relations of **F**, **R**, and **U**, the author developed a c++ code to calculate

R from **F**. (Note that **F**, **R**, **U** are all 3x3 matrix.)

F = **RU**

C = **FF**^{T} = **U**^{2}

R = **FU**$^{-1}$

And microrotation vector $\phi_k = \frac{1}{2}\epsilon_{ijk}(R_{skew})_{ij}$

Where $R_{skew} = \frac{1}{2}(R - R^T)$

$$\epsilon_{ijk} = \begin{cases} +1, & when\ ijk\ is\ an\ even\ permutation\ of\ 1,2,3 \\ -1, & when\ ijk\ is\ an\ odd\ permutation\ of\ 1,2,3 \\ 0, & when\ any\ indices\ are\ equal \end{cases}$$

i.e.   ijk = 123, 312, 231… ϵ_{ijk} = 1;

              ijk = 213, 132… ϵ_{ijk} = -1;

The basic structure of the MR calculation code is demonstrated below:

```
double (double F[3][3])
{
    double r[3][3],C[3][3],u1[3][3],R[3][3];
    double microrotation;

            M_T(F,r);                           //Trans
            MM(F,r,C);                           //C=F F^T
            U_1(C, u1);                          //u1u1=C
            MM(F,u1,R);                          //R=F u1
            M_T(R,r);                            //Trans
            mr[0] = (R[1][2] - r[1][2])/2;
            mr[1] = (R[2][0] - r[2][0])/2;
            mr[2] = (R[0][1] - r[0][1])/2;
        microrotation = sqrt(pow(mr[0],2)+pow(mr[1],2)+pow(mr[2],2))
    return microrotation;
}
int M_T(double a[3][3], double r[3][3])
{
        int i,j;
        for(i=0;i<3;i++)
        for(j=0;j<3;j++)
        r[i][j] = a[j][i];
        return 0;
}
double tr(double a[3][3])
{
        double t;
        t = a[0][0] + a[1][1] + a[2][2];
        return t;
```

```
}

double det(double a[3][3])

{        double t;

         t    =    (a[0][0]*a[1][1]*a[2][2])    +    (a[0][1]*a[1][2]*a[2][0])    +
(a[0][2]*a[1][0]*a[2][1])  -  (a[0][0]*a[1][2]*a[2][1])  -  (a[0][1]*a[1][0]*a[2][2])  -
(a[0][2]*a[1][1]*a[2][0]);

         return t;

}

int MM(double a[3][3], double b[3][3], double r[3][3])

{

         int i,j,k;

         for(i=0;i<3;i++)

         for(j=0;j<3;j++)

         {         r[i][j] = 0;

                   for(k=0;k<3;k++) r[i][j] = r[i][j] + (a[i][k]*b[k][j]);

         }

         return 0;

}

int U_1(double C[3][3], double u1[3][3])

{

         double Ic[3],Iu[3],k,t, ec[3],ev[3],u[3][3];

         double r[3][3];

         int i,j;

         double l,p,coso[3], sino;

         int kk = 0;

         for(j=0;j<3;j++)

         for(i=0;i<3;i++)

          u1[j][i] = 0;

         MM(C,C,r);

         Ic[0] = tr(C);
```

```
Ic[1] = pow(Ic[0],2) - tr(r);

Ic[1] = Ic[1]/2;

Ic[2] = det(C);

for(i=0;i<3;i++) if(fabs(Ic[i]) < 1E-5) {

    Ic[i] = 0;kk++;

    }

k = pow(Ic[0],2)-Ic[1]*3;

if(k < TINY || kk > 1)

{

        ec[0] = sqrt(Ic[0]/3);

        for(i=0;i<3;i++)

        for(j=0;j<3;j++)

                    if(i == j) u1[i][j] = ec[0];

        return 1;

}

l = pow(Ic[0],3)-Ic[0]*Ic[1]*9/2+Ic[2]*27/2;

t = pow(k,1.5);

t = (l/t);

if(t < 1+TINY && t > 1-TINY) p = 0;

else p = acos(t);

coso[0] = cos(p/3);

sino = sqrt(1-pow(coso[0],2));

coso[1] = 0-(coso[0] + sqrt(3)*sino)/2;

coso[2] = 0-(coso[0] - sqrt(3)*sino)/2;

for(i=0;i<3;i++) {

    ev[i] = sqrt((Ic[0] + 2*sqrt(k)*coso[i])/3);}

Iu[0] = ev[0]+ev[1]+ev[2];

Iu[1] = (ev[0]*(ev[1]+ev[2])) + (ev[1]*ev[2]);

Iu[2] = ev[0]*ev[1]*ev[2];

for(i=0;i<3;i++)
```

```
        for(j=0;j<3;j++)

        {

                u[i][j] = (1/(Iu[0]*Iu[1] - Iu[2]))*(Iu[0]*Iu[2]*I[i][j] + (Iu[0]*Iu[0] -
        Iu[1])*C[i][j] - r[i][j]);

                u1[i][j] = (1/Iu[2])*(Iu[1] * I[i][j] - Iu[0] * u[i][j] + C[i][j]);

        }

        return 0;

}
```

Dilatation

Dilatation is the first invariant of the Green Strain Tensor (**E**), and dilatation estimates the atomic strain. Dilatation calculations are also based on Deformation Gradient:

$$E = \frac{1}{2}(F^T F - I) \text{ and } e = \text{tr(E)}$$

I is the identity tensor $= \begin{pmatrix} 1 & 0 & 0 \\ 0 & 1 & 0 \\ 0 & 0 & 1 \end{pmatrix}$

Also, based on the relations above, the dilatation calculation code would be:

```
double dilitation(double F[3][3])

{       int i,j;

        double e=0;

        for(i=0;i<3;i++)

        for(j=0;j<3;j++){

            if(i==j) e = e + pow(F[i][j],2);}

        e = (e-3)/2;
```

> *return e;*

}

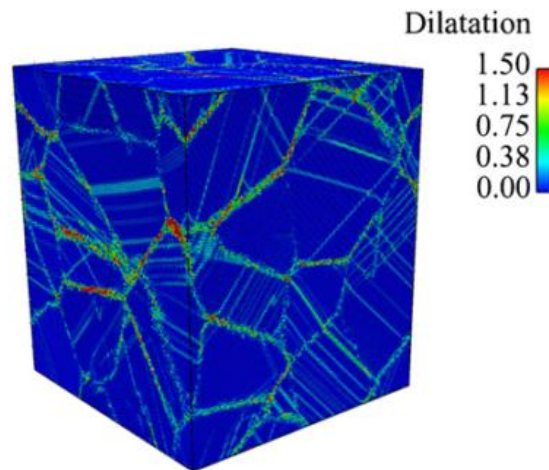All of these metrics will show a complete image of the state, from structure to deformation status.

Figure 24   Snapshots of 15nm grained NC Cu at 10% tensile strain colored by dilatation. [From: G.J. Tucker et al. / J. Mech. Phys. Solids 60 (2012)]

Nanoindentation on NC Ni and Ni 1 at. % P

As discussed above, the detailed mechanisms of stress-assisted grain growth has yet to be explained clearly. We propose the use of atomistic simulations to elucidate the contributions to this kind of grain growth, employing LAMMPS to perform experiments on 4 samples:

S1   3nm grained pure Ni, indent at 300K

S2   6nm grained pure Ni, indent at 300K

S3   3nm grained pure Ni, indent at 10K

S4 3nm grained Ni 1 at. % P, indent at 300K

For these 4 samples, we apply r = 15nm indenter, and indent to 5nm depth with an indentation speed of 5m/s.

Procedure

Potential Selection

We chose to use the potential from reference [26] for our pure Ni samples, and use reference [44] for our NiP sample.

Structure Building

The initial structure of the samples are all 50x50x50 nm^3; and by controlling the number of grains, we made 3nm grained samples and 6nm grained samples. All samples are pure Ni at this stage.

Preparation of the samples

1. Before indentation, S2 is annealed at 1175K for 0.2ns.

2. Before indentation, S1 and S3 are annealed at 650K for 0.2ns. (Higher temperature will damage the structure, causing the grain to grow rapidly to approximately 5nm.)

3. 1% of S4 atoms are replaced with P randomly and then we applied the Scalable Monte Carlo procedure [40] to reduce the system energy. When approaching the equilibrium state, most of the P atoms segregate into the grain boundaries, shown in Figure.25.
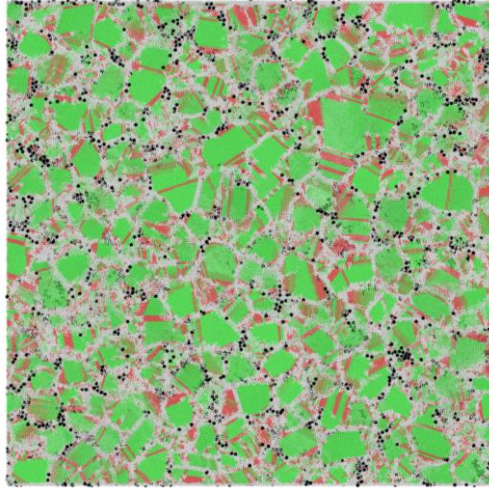
Figure 25　S4 structure after MC process. Black dots are P atoms, others are Ni atoms colored by CNA: green atoms are FCC, white atoms are grain boundaries, and red atoms are HCP.

4.　After the MC process, sample S4 is annealed at 650K for 0.2ns.

Nanoindentation

The spherical indenter size is set to r = 15nm with an indenting speed of 5m/s.

Before indentation, the top and bottom surfaces transfer to a free surface, transforming the entire structure to a film. During indentation, the environmental temperature is set to be 300K for S1, S2 and S4, while 10K for S3.

A sample script is shown below:

 # Indentation for Ni
 # Yang Zhang
 # ---------- Initialize Simulation --------------------
clear
units　　　　　　　metal
dimension　　　　　3
boundary　　　　　　pp pp pp
atom_style　　　　　atomic

```
atom_modify            map array
# ---------- Define Interatomic Potential ---------------------
pair_style eam/alloy
read_data               Ni_3nm.data
pair_coeff              * * Ni.set Ni
neighbor                 2.0 bin
neigh_modify            every 1 delay 25 check yes
# ---------- Run Simulation ---------------------
reset_timestep 0
timestep 0.002
change_box all z delta -6.0 6.0 boundary p p s
fix 4 all indent 10.0 plane z -250 lo units box
variable zup equal "250 + 150.0 - 0.05*step*dt"
fix 5 all indent 10.0 sphere 0.0 0.0 v_zup 150.0 units box
fix 6 all npt temp 10 10 1.0 x 0.0 0.0 1.0 y 0.0 0.0 1.0
dump 6 all custom 10000 INDD.Ni10k.* id type x y z
thermo 5000
thermo_style custom step temp pe ke etotal press vol lx ly lz pxx pyy pzz
restart 10000 restart.Ni3nm.EM4.*
run 500000
unfix 5
unfix 6
undump 6
print "All done!"

# End
```

This script will indent to a depth of ~5nm and provide snapshots for analysis.
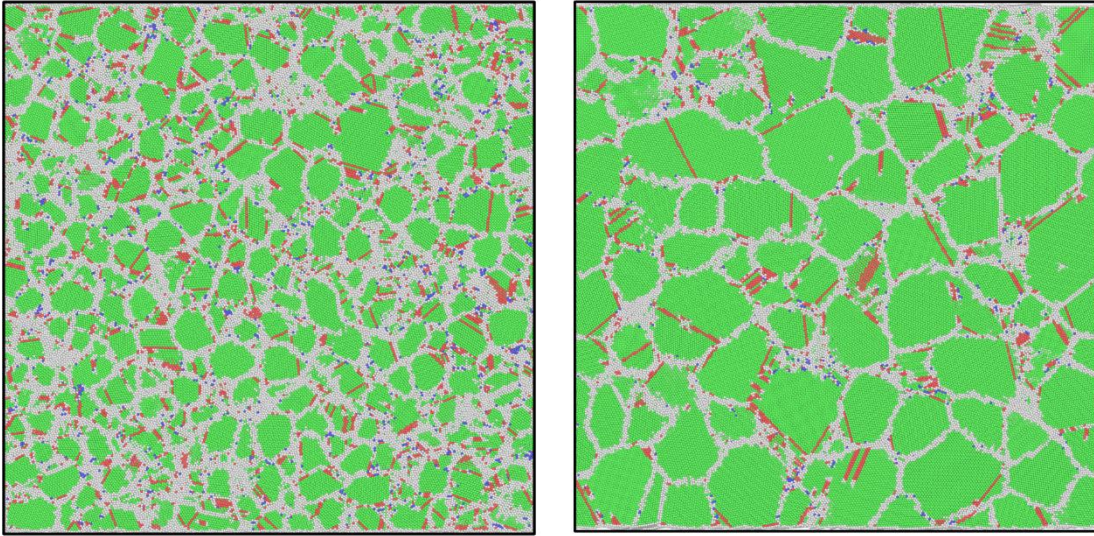
Data Analysis

Figure 26   Sectional view of S1 and S2 respectively as-annealed colored by CNA. Green for FCC, White for Grain Boundaries, Red for HCP, Blue for BCC.
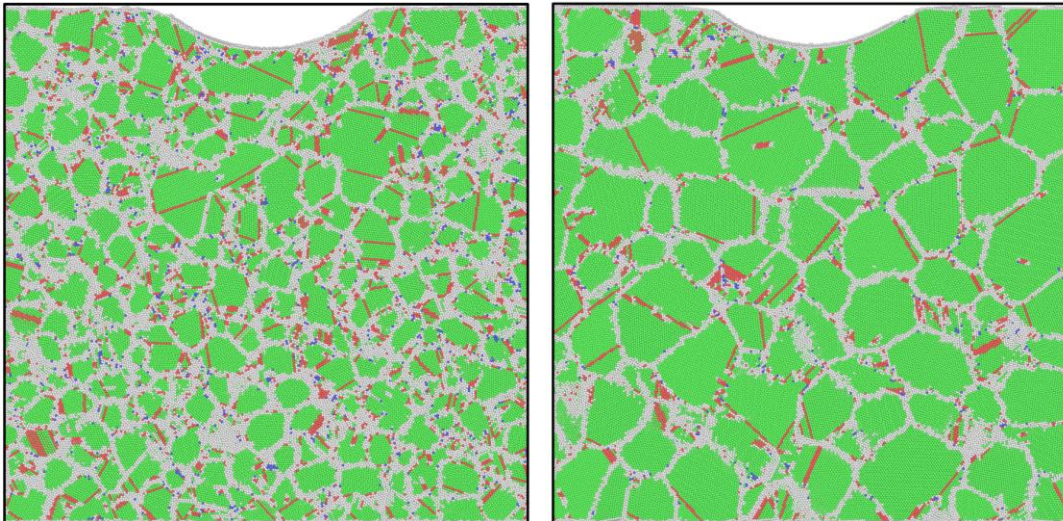

Figure 27   Sectional view of S1 and S2 respectively at the indent depth of 5nm colored by CNA. Green for FCC, White for Grain Boundaries, Red for HCP, Blue for BCC

It is difficult to observe any detailed mechanisms from deformation snapshots using the common neighbor analysis visualization. Therefore, a numerical analysis is required to confirm what changes occur in these structures.

Grain Size Evolution

Normalized Average Grain Size of Each Sample
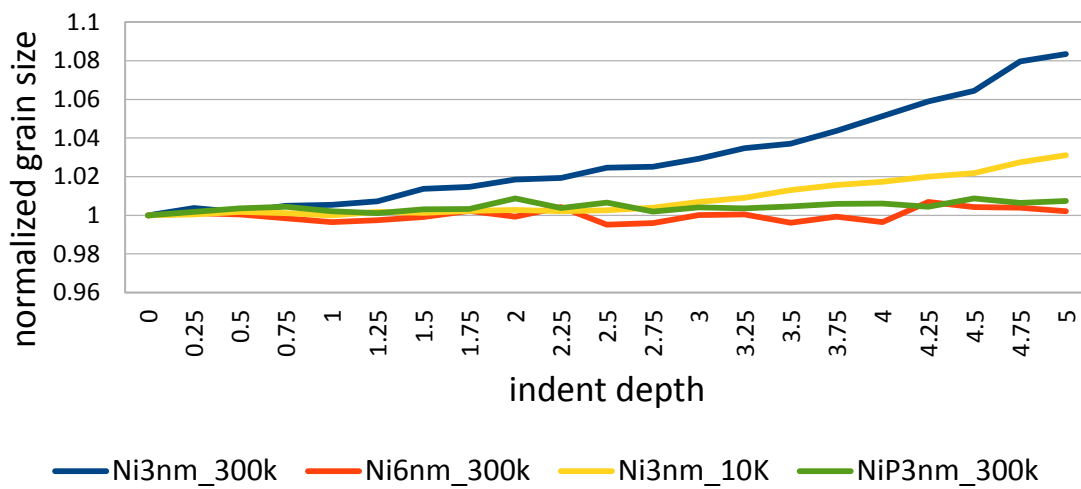
We applied a grain size calculation algorithm to every snapshot of every sample. The results show that the highest grain growth is observed in sample S1, while sample S3 exhibits more subtle growth, and S2 and S4 almost no grain growth.

The calculation computes the normalized grain size $\frac{D_s}{D_0}$, where D_s is the average grain size of the snapshot, and D_0 is the average grain size of initial state.

Then, we divided the sample into two parts based on the assumed stress field according to Hertzian contact mechanics [45], which ensures that at 5nm indent depth, the "high stress" region would have the highest stress greater than 0.07 Pm (the maximum pressure), and the "low stress" region would have stresses less than 0.07 Pm.
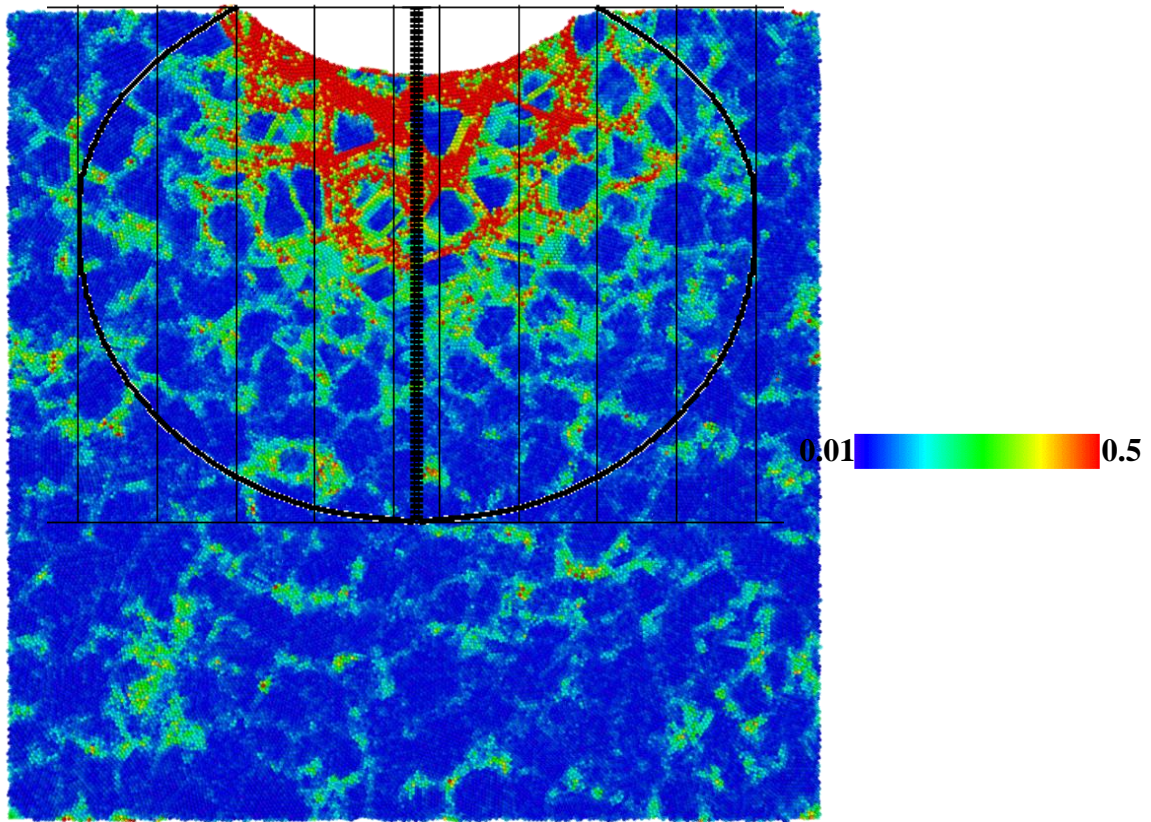
39

Figure 28   S1 sample at 5nm indent depth colored by atomic strain. The circle divides the structure into a High Stress region and a Low Stress region.

After we divided the structure into a high stress region and a low stress region, we recalculated the grain size in each and found out that most of the grain growth occurred in the HS region, confirming that this kind of grain growth is stress-assisted.
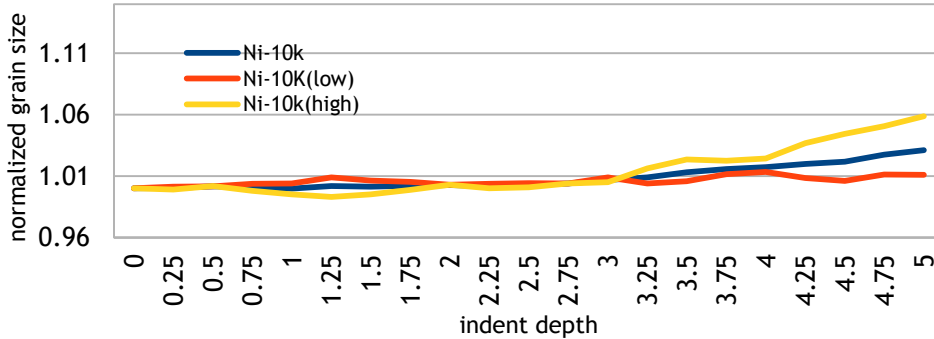
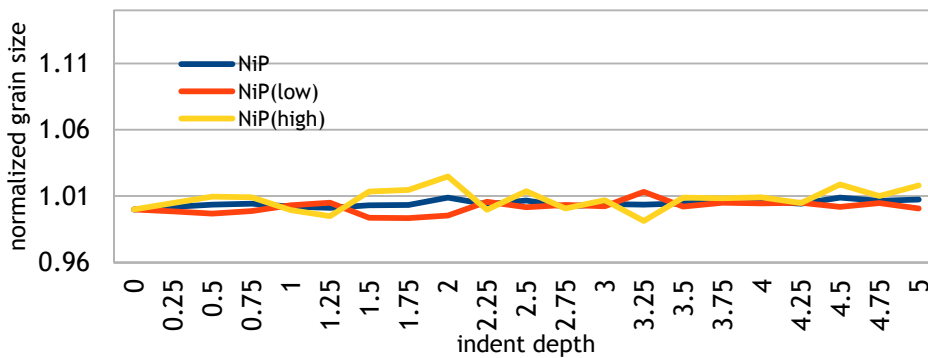Normalized Average Grain Size of different regions in S1
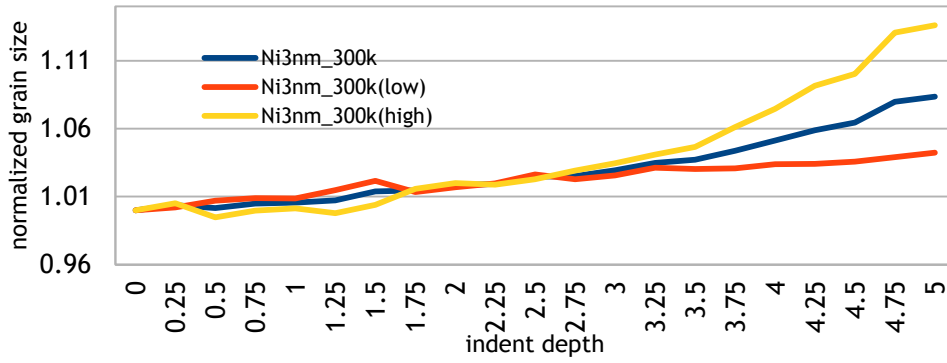
Normalized Average Grain Size of different regions in S2
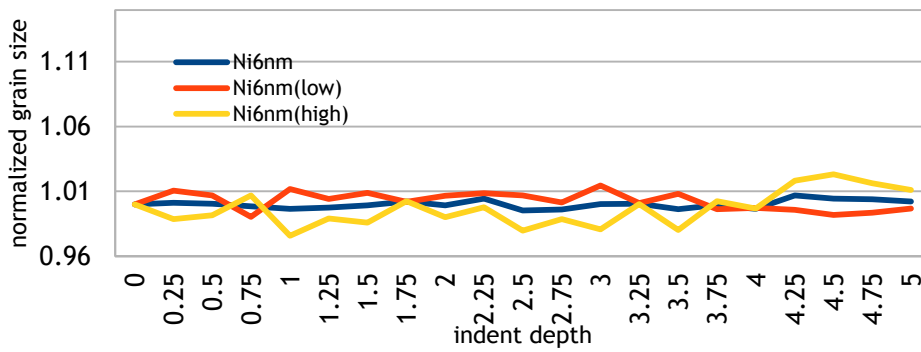
Normalized Average Grain Size of different regions in S3

Normalized Average Grain Size of different regions in S4
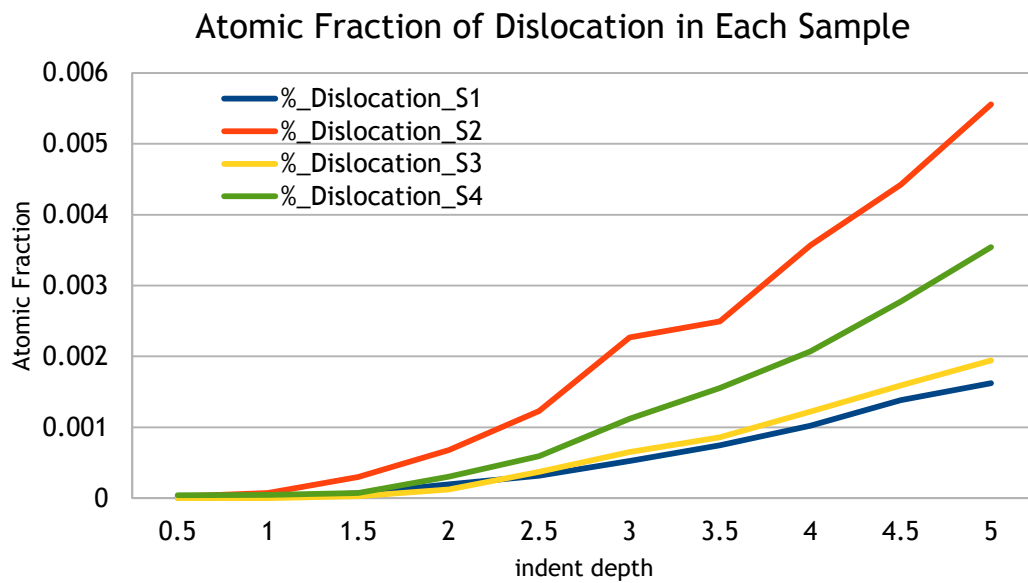
Atomic Fraction of Dislocation

Figure 29   Atomic fraction of dislocation atoms, the graph shows that the dislocations multiply best in S2 for biggest grain size, and better in S4 for impurity atoms. Dislocations multiply slightly better in S3 when compared to S1 for the brittleness increasing at low temperature.

Next, we performed a slip vector calculation, counting the number of dislocation atoms in each snapshot. In S2 and S4, the atomic fraction of dislocations is much higher than in S1 and S3. This indicates that much more energy is used to initiate and multiply dislocations in samples S2 and S4 in comparison to S1 and S3.

Figure.29 is applicable for the following reason:

1. S2 has the largest grain size, so dislocations will not meet as many grain boundaries when compared to other samples.

2. S4 has impurities which will likely form "vacancies" and/or stacking faults because of the non-uniform chemical potential distribution and/or different atomic radius.

3. S3 was deformed at extremely low temperature, hence even though intrinsic dislocations initiated by thermal energy is lower than in S1, their multiplication is more rapid in S3. It is evident in Figure 29 before 2.5nm indent depth, S1 contains more dislocations than S3. However, a transition occurs at a depth around 2.3 nm where the atomic fraction of dislocation atoms in S3 is enhanced at larger depths.

This not only shows dislocation behavior, but also when compared with grain size evolution figures, indicates that the driving energy from the indenter separates into 2 parts: dislocation initiation and grain growth accommodated by grain coalescence.

Rotate and Coalesce Mechanism

Next, a few grains are focused on to elucidate the mechanisms accommodating stress assisted grain growth at the nanoscale, as follows in Figure 30.
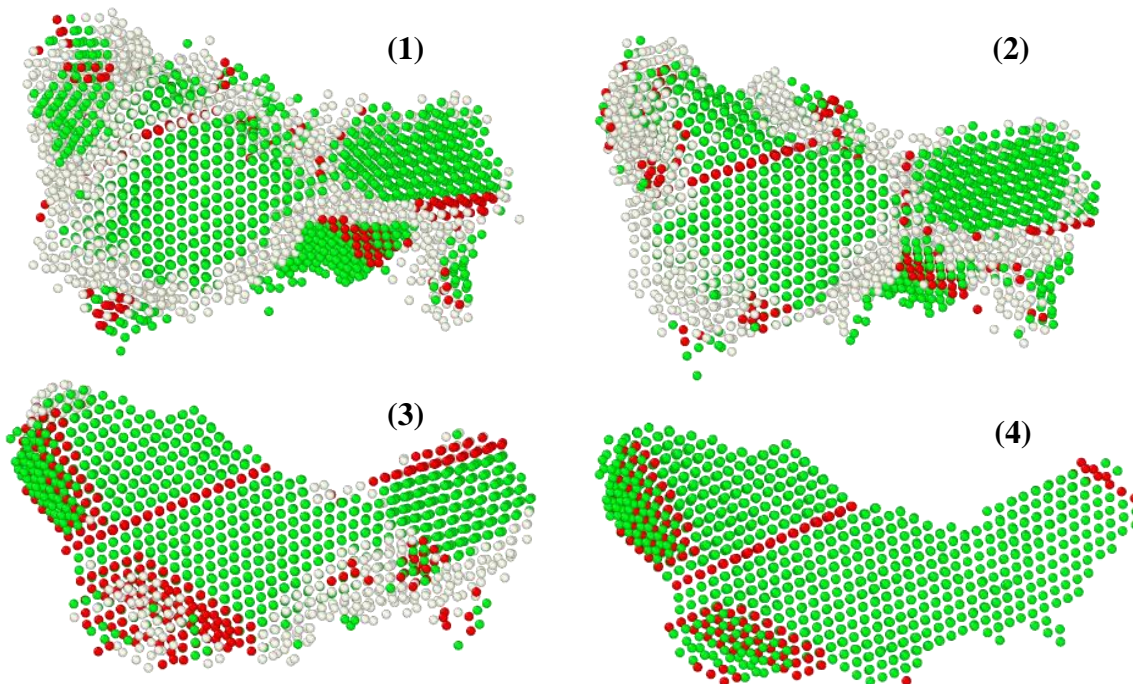

Figure 30　Zoom-in observation of the grain growth process [from (1) to (4)] colored by CNA, Green for FCC, White for GB, Red for HCP. In the initial structure (1), the neighbor grains are all of different orientations from the central grain. However, neighbor grains gradually rotate into the right orientation, and finally coalesce to one grain, leaving some stacking faults on the boundaries baring very high mis-orientation angle.

From Figure 30-(1) to (4), several grains gradually rotate to a single orientation system and coalesce into a single grain leaving some stacking faults at the boundaries with high misorientation angles. The rightmost grain continuously changes its orientation to align with the central grain, and finally succeeds to rotate to the same orientation as the central grain leading to the coalescence and growth processes.
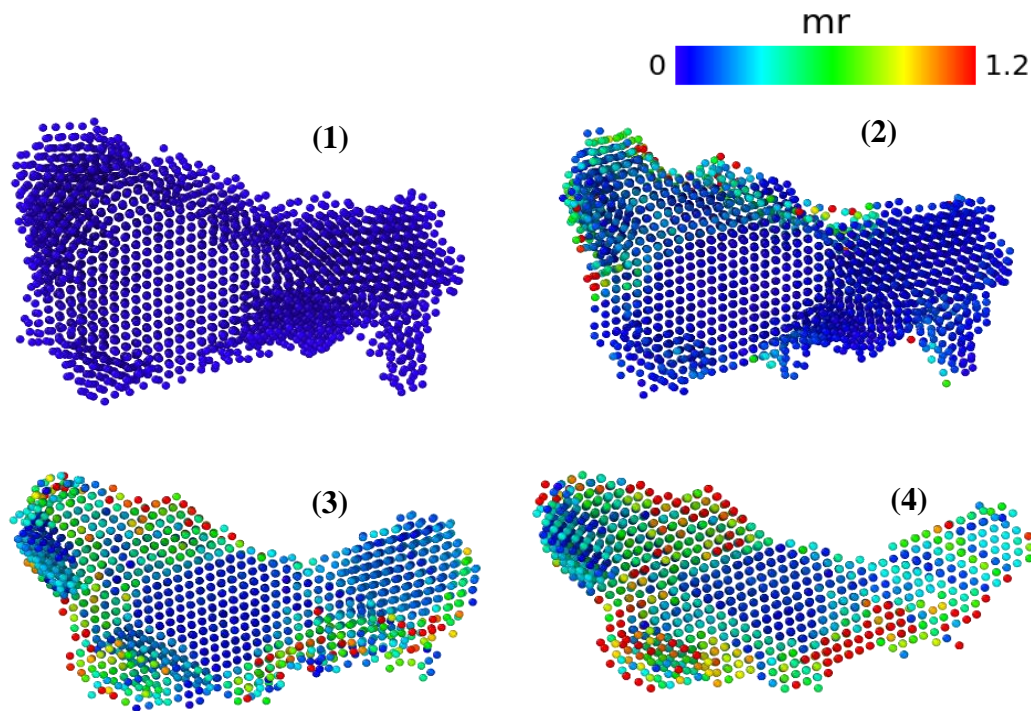

Figure 31 Zoom-in observation of the grain growth process [from (1) to (4)] colored by Micro-Rotation taking the reference state as (1). It is even clearer when colored by MR that the grains are really rotating, and for different regions the rotation degrees are different.

Then, we performed micro-rotation calculations for these grains [the reference state is (1)], which uncovered that the grains are heavily rotated, rotation occurs prior to coalescence, and both the boundaries and grain interiors exhibited varying degrees of rotation. Thus, primary mechanisms accommodating stress-assisted grain growth is the rotation and coalescence mechanism.

Finally, it is important to note that the 6nm grain size sample (S2) and solute grain boundary

segregated sample (S4) exhibited very limited growth relative to the 3 nm Ni grain size sample. Thus although the mechanical driving force is present, the 6 nm structure is not in a high enough energy state for grain growth to occur whereas the P located at the grain boundaries in the Ni-P structure inhibit rotation of the grain boundary atoms.
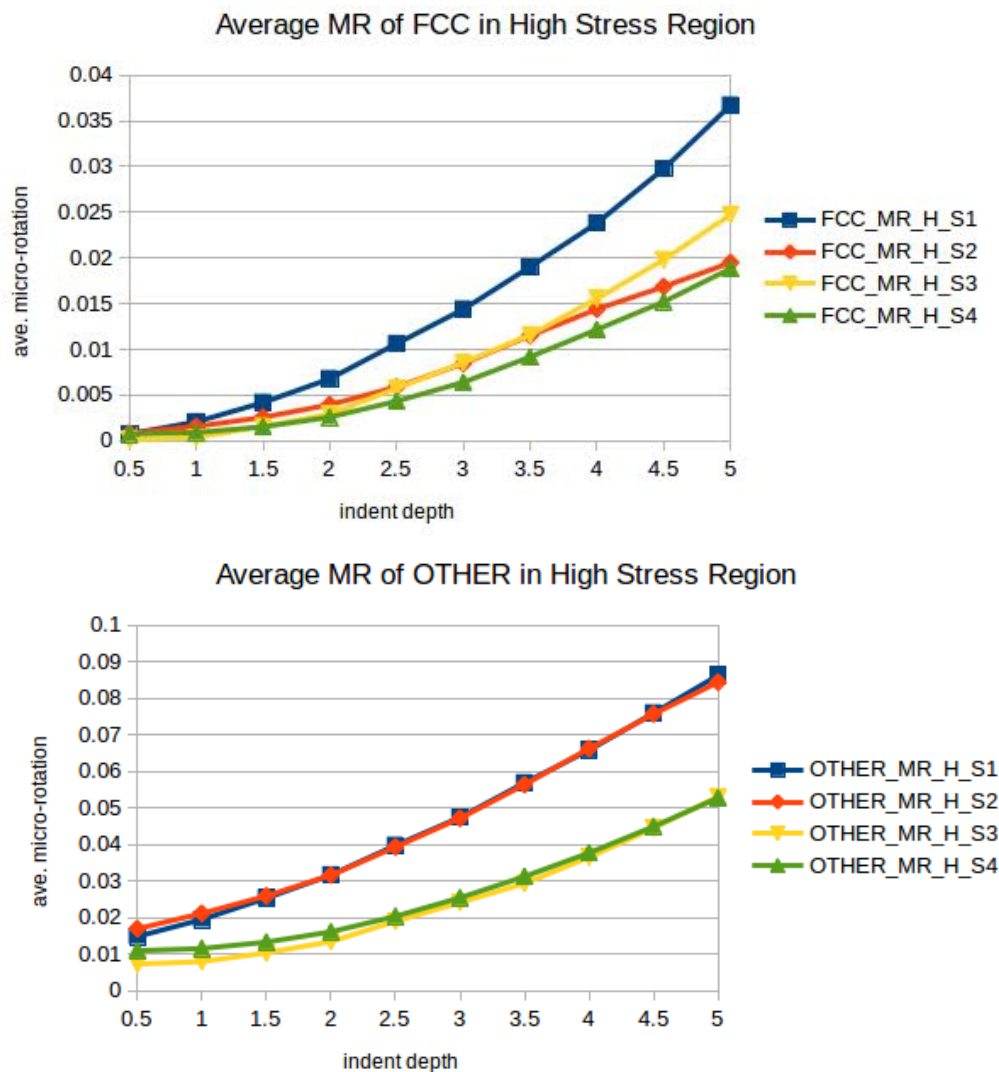
Average Micro-Rotation in HS region.

Figure 32   Average MR of FCC and OTHER atoms in the High Stress Region.

The average micro-rotation for GIs (FCC atoms) and GBs (OTHER atoms) were calculated as

shown in Figure 32. In S1, GIs and GBs both ehibit a high degree of rotation, and correspondingly demonstrated the most prominent grain growth. Although in S2, GBs rotate more than S3, when S3's average FCC MR value exceeds that of S2 at approximately a 3nm indent depth, grain growth in S3 became enhanced while the reduced FCC MR Value of S2 corresponded to diminished grain growth.

Average Dilatation in HS region

As we've observed in the rotate and coalesce mechanism section, pure rotation cannot lead directly to grain coalescence. After rotation, the atoms need to rearrange themselves to fit in the crystalline lattice. Thus, dilatation accompanies the rotation mechanisms as illustrated in Figure 33.
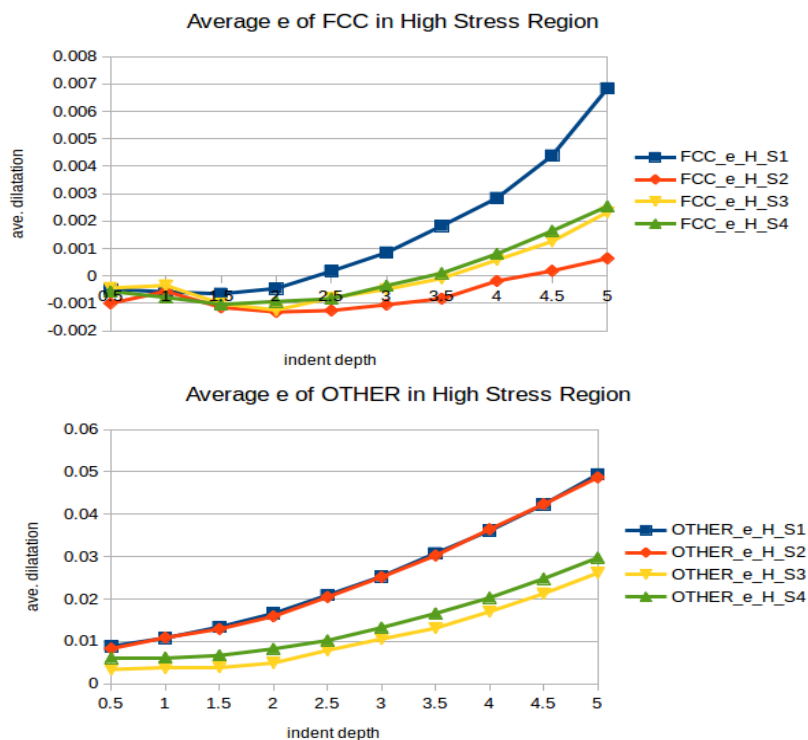

Figure 33   Average dilatation of FCC and OTHER atoms in the High Stress Region

For this close packed system, GBs are moving around far more easily than GIs (~10 times).

However, for the sample with most grain growth (S1), GIs rearrange themselves more often than in other samples. The high value of dilatation in S4 is already explained, and it should be the same process with the dislocation mechanism: the impurities cause "vacancies" and stacking faults in the grains. For S2 and S3, I think the previous explanation is enough.

The Thermal Component of Deformation

Equation (5) shows how temperature affects the grain growth rate.

$$t = \frac{d_0^n [1+(1+x)^n]}{K_0 exp\left(\frac{-Q}{RT}\right)} \tag{5}$$

It really makes sense and the observations in this simulation experiment can provide a more detailed description with S1 and S3, because the only variable for them is temperature.

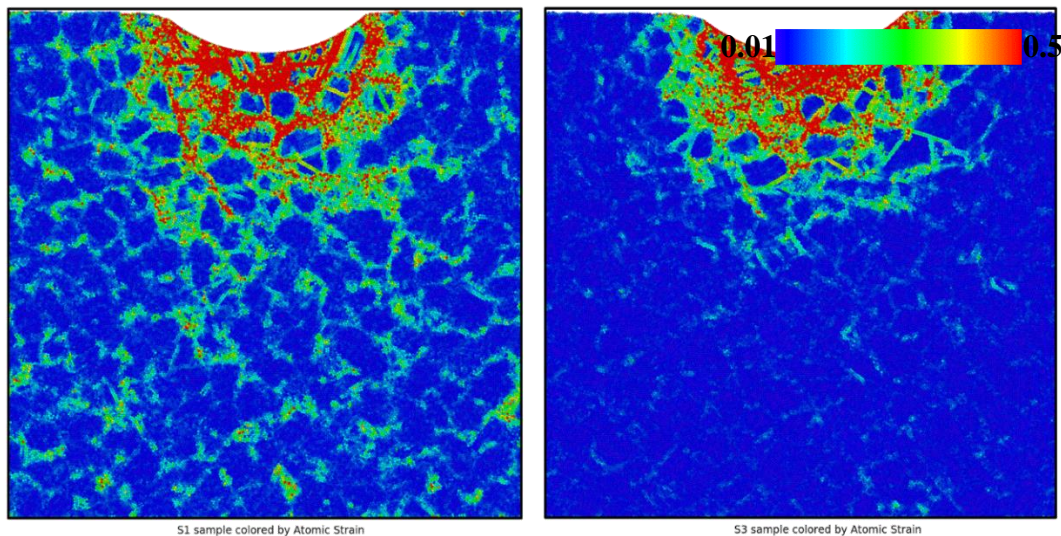Figure 34   S1 and S3 structure at 5nm indent depth colored by Atomic Strain. Left is S1 sample which is indented at 300K, while the right S3 sample is indented at 10K.

Deformation is highly localized in S3 at an extremely low temperatures, whereas in S1 at 300K, a much larger region is activated. A quantitative representation of this localized deformation volume in S3 is to examine the dilatation distribution, as shown in Figure 35.
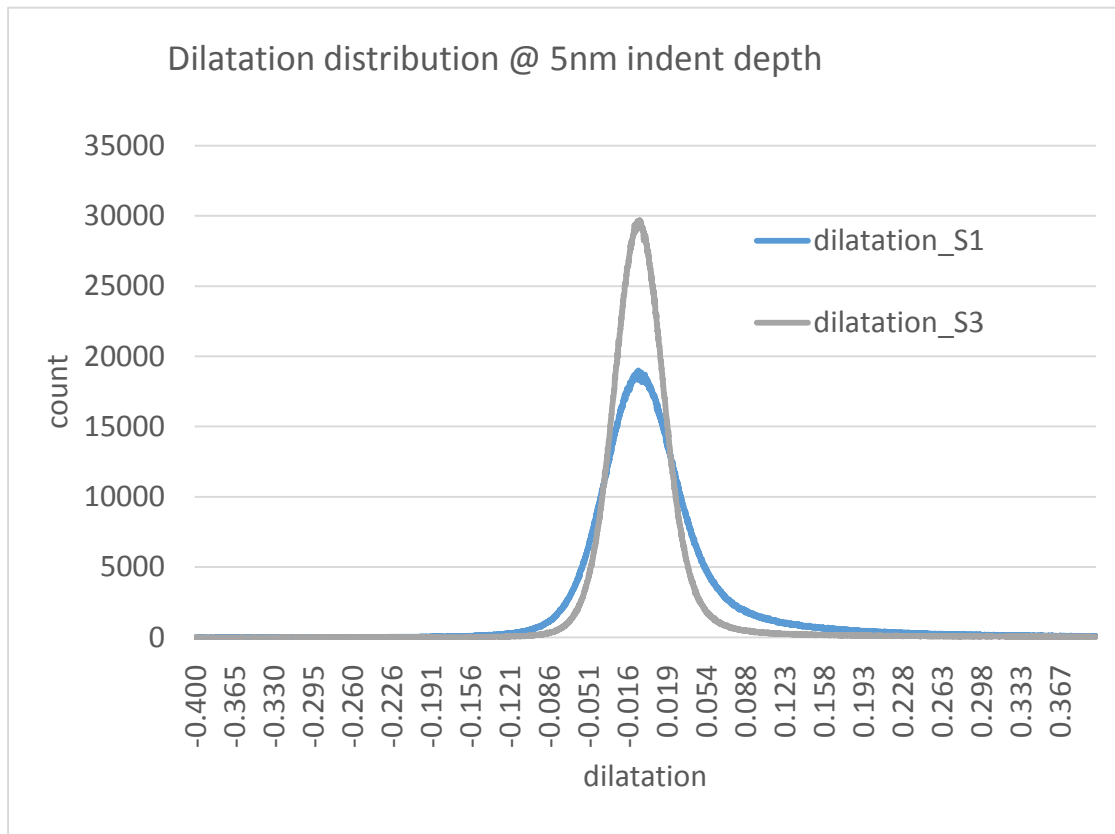
The graph alone tells the complete story: much more atoms are activated at 300K than at 10K. More atoms bare high energy/deformation at 300K in S1 than at 10K in S3. As the structure holds more high energy parts, it will be more likely to deform; however, as grain growth can reduce the energy of the system, it will become the dominant mechanism in structures with a high density of grain boundaries not stabilized by solute. Thus, these higher energy states can be expected to exhibit stress-assisted grain growth, which will ultimately have implications for macroscopic mechanical properties such as strength, toughness, and ductility.

Concluding Remarks

In this work, we observed grain growth on the atomic scale, and confirmed by deformation metrics that it can be highly accelerated by stress. One of the mechanisms for stress-assisted grain growth would be rotate and coalesce mechanism. Stress, along with temperature, grain

boundary segregation, and the initial structure, influence the rate of grain growth. The grain

growth function $t = \dfrac{d_0^n[1+(1+x)^n]}{K_0 exp\left(\frac{-Q}{RT}\right)}$ can still capture phenomena observed during the

atomistic simulations, and future work should focus on quantifying the activation energy of

stress-assisted grain growth accommodated by the grain rotation and coalescence mechanism.

References

1. K.Lu, *Nanocrystalline metals crystallized from amorphous solids: nanocrystallization, structure, and properties.* materials Science and Engineering, 1996. **R16**.

2. Valiev, R.Z., *Structure and mechanical properties of ultrafine-grained metals.* Materials Science and Engineering: A, 1997. **234**.

3. Mukherjee, A.V.S.V.V.S.R.Z.V.A.K., *Advanced mechanical properties of pure titanium with ultrafine grained structure.* Scripta Materialia, 2001. **45**.

4. Hanamura, T. and H. Qiu, *Ultra-Fine Grained Steel: Relationship Between Grain Size and Tensile Properties.* 2014: p. 9-25.

5. Meyers, M.A., A. Mishra, and D.J. Benson, *Mechanical properties of nanocrystalline materials.* Progress in Materials Science, 2006. **51**(4): p. 427-556.

6. Dalla Torre, F., et al., *Microstructures and properties of copper processed by equal channel angular extrusion for 1–16 passes.* Acta Materialia, 2004. **52**(16): p. 4819-4832.

7. Weins, M.J., *Computer Calculations of the Structure and Energy of High-Angle Grain Boundaries.* Journal of Applied Physics, 1971. **42**(7): p. 2639.

8. Palumbo G, Thorpe SJ, Aust KT., On the contribution of triple junctions to the structure and properties of nanocrystalline materials, Scripta Metall Mater 1990;24:1347–50

9. ErIas.C.AIFANTIS, *The Physics of plastic deformation.* International Journal of Plcsticity, 1987. **3**.

10. Wu, X., et al., *Nanodomained Nickel Unite Nanocrystal Strength with Coarse-Grain Ductility.* Sci Rep, 2015. **5**: p. 11728.

11. Mike Gedeon, Brush Wellman's Alloy Customer Technical Service Department

12. A.H.Chokshi, et al., *ON THE VALIDITY OF THE HALL-PETCH RELATIONSHIP IN NANOCRYSTALLINE MATERIALS.* Scripta Materialia, 1989. **23**: p. 5.

13. C.Suryanarayana and C.C.Koch, *Nanocrystalline materials-Current research and future directions.* Hyperfine Interactions, 2000. **130**.

14. S.X.McFadden, et al., *Low-temperature superplasticity in nanostructured nickel and*

metal alloys. Nature, 1999. **398**.

15. Gleiter, H., *NANOCRYSTALLINE MATERIALS.* Progress in Materials Science, 1989. **33**.

16. C.Suryanarayana, *Nanocrystalline Materials.* international materials reviews, 1995. **40**.

17. Trelewicz, J.R. and C.A. Schuh, *The Hall–Petch breakdown in nanocrystalline metals: A crossover to glass-like deformation.* Acta Materialia, 2007. **55**(17): p. 5948-5958.

18. Morris DG., Mechanical behavior of nanostructured materials. Trans Tech Publication Ltd; 1998

19. Suryanarayana, C., *Mechanical alloying and milling.* Progress in Materials Science, 2001. **46**.

20. Detor, A. and C. Schuh, *Grain boundary segregation, chemical ordering and stability of nanocrystalline alloys: Atomistic computer simulations in the Ni–W system.* Acta Materialia, 2007. **55**(12): p. 4221-4232.

21. Ruslan.Z.Valiev, et al., *Producing Bulk Ultrafine-Grained Materials by Severe Plastic Deformation.* Jom, 2006.

22. Catherine.C.Berry and Adam.S.G.Curtis, *Functionalisation of magnetic nanoparticles for applications in biomedicine.* Journal of Physics D: Applied Physics, 2003. **36**.

23. Lu, A.H., E.L. Salabas, and F. Schuth, *Magnetic nanoparticles: synthesis, protection, functionalization, and application.* Angew Chem Int Ed Engl, 2007. **46**(8): p. 1222-44.

24. Gao, J., H. Gu, and B. Xu, *Multifunctional magnetic nanoparticles: design, synthesis, and biomedical applications.* Acc Chem Res, 2009. **42**(8): p. 1097-107.

25. McHenry, M.E. and D.E. Laughlin, *ChemInform Abstract: Nano-Scale Materials Development for Future Magnetic Applications.* ChemInform, 2010. **31**(22): p. no-no.

26. Zhou, X.W., R.A. Johnson, and H.N.G. Wadley, *Misfit-energy-increasing dislocations in vapor-deposited CoFe/NiFe multilayers.* Physical Review B, 2004. **69**(14).

27. Charles.R.Martin, *Nanomaterials--A Membrane-Based Synthetic Approach.* Science, 1994.

28. Sun, S., *Recent Advances in Chemical Synthesis, Self-Assembly, and Applications of FePt Nanoparticles.* Advanced Materials, 2006. **18**(4): p. 393-403.

29. SUN, F., et al., *Thermal Stability and Recrystallization of Nanocrystalline Ti Produced by Cryogenic Milling.* metallurgical and Materials Transactions A, 2006. **37A**.

30. T.R. Malow and C.C. Koch, Synthesis and Processing of Nanocrystalline Powder,ed. D.L.Bourell (TMS,Warrendale, PA, 1996) .

31. R.W. Siegel, Materials Interfaces: Atomic Level Structure and Properties, eds. D. Wolf and S. Yip (Chapman & Hall, London, UK, 1992)

32. Okamoto, H., *Phase Diagrams for Binary Alloys.* ASM International, 2010.

33. C.E. Krill, R. Klein, S. Janes and R. Birringer, Mater. Sci. Forum (1995) 443.

34. Koch, C.C., et al., *Stabilization of nanocrystalline grain sizes by solute additions.* Journal of Materials Science, 2008. **43**(23-24): p. 7264-7272.

35. Jin, M., et al., *Direct observation of deformation-induced grain growth during the nanoindentation of ultrafine-grained Al at room temperature.* Acta Materialia, 2004. **52**(18): p. 5381-5387.

36. Lin, Y., et al., *Stress-Induced Grain Growth in an Ultra-Fine Grained Al Alloy.* Metallurgical and Materials Transactions A, 2014. **45**(6): p. 2673-2688.

37. Stukowski, Structure identification methods for atomistic simulations of crystalline materials, Modell. Simul. Mater. Sci. Eng. 20, 045021

38. Zimmerman, J.A., et al., *Calculation of stress in atomistic simulation.* Modelling and Simulation in Materials Science and Engineering, 2004. **12**(4): p. S319-S332.

39. Traiviratana, S., et al., *Void growth in metals: Atomistic calculations.* Acta Materialia, 2008. **56**(15): p. 3874-3886.

40. Sadigh.Babak, et al., *Scalable parallel Monte Carlo algorithm for atomistic simulations of precipitation in alloys.* Physical Review B, 2012. **85**(18).

41. Tucker, G.J., et al., *Investigating the deformation of nanocrystalline copper with microscale kinematic metrics and molecular dynamics.* Journal of the Mechanics and Physics of Solids, 2012. **60**(3): p. 471-486.

42. Zimmerman, J.A., D.J. Bammann, and H. Gao, *Deformation gradients for continuum mechanical analysis of atomistic simulations.* International Journal of Solids and Structures, 2009. **46**(2): p. 238-253.

43. Tucker, G.J., J.A. Zimmerman, and D.L. McDowell, *Shear deformation kinematics of*

bicrystalline grain boundaries in atomistic simulations. Modelling and Simulation in Materials Science and Engineering, 2010. **18**(1): p. 015002.

44.   Sheng, H.W., E. Ma, and M.J. Kramer, *Relating Dynamic Properties to Atomic Structure in Metallic Glasses.* Jom, 2012. **64**(7): p. 856-881.

45.   Anthony.C.Fischer-Cripps, *Introduction to Contact Mechanics.* 2006.